

## DEBRIS DISK EVOLUTION AROUND A STARS

K. Y. L. SU<sup>1</sup>, G. H. RIEKE<sup>1</sup>, J. A. STANSBERRY<sup>1</sup>, G. BRYDEN<sup>2</sup>, K. R. STAPELFELDT<sup>2</sup>, D. E. TRILLING<sup>1</sup>, J. MUZEROLLE<sup>1</sup>,  
C. A. BEICHMAN<sup>2,3</sup>, A. MORO-MARTIN<sup>4</sup>, D. C. HINES<sup>5</sup>, M. W. WERNER<sup>2</sup>

*accepted for publication in ApJ*

### ABSTRACT

We report 24 and/or 70  $\mu\text{m}$  measurements of  $\sim 160$  A-type main-sequence stars using the Multiband Imaging Photometer for *Spitzer* (MIPS). Their ages range from 5 to 850 Myr based on estimates from the literature (cluster or moving group associations) or from the H-R diagram and isochrones. The thermal infrared excess is identified by comparing the deviation ( $\sim 3\%$  and  $\sim 15\%$  at the  $1\text{-}\sigma$  level at 24 and 70  $\mu\text{m}$ , respectively) between the measurements and the synthetic Kurucz photospheric predictions. Stars showing excess infrared emission due to strong emission lines or extended nebulosity seen at 24  $\mu\text{m}$  are excluded from our sample; therefore, the remaining infrared excesses are likely to arise from circumstellar debris disks. At the  $3\text{-}\sigma$  confidence level, the excess rate at 24 and 70  $\mu\text{m}$  is 32% and  $\geq 33\%$  (with an uncertainty of 5%), considerably higher than has been found for old solar analogs and M dwarfs. Our measurements place constraints on the fractional dust luminosities and temperatures in the disks. We find that older stars tend to have lower fractional dust luminosity than younger ones. While the fractional luminosity from the excess infrared emission follows a general  $1/t$  relationship, the values at a given stellar age vary by at least two orders of magnitude. We also find that (1) older stars possess a narrow range of temperature distribution peaking at colder temperatures, and (2) the disk emission at 70  $\mu\text{m}$  persists longer than that at 24  $\mu\text{m}$ . Both results suggest that the debris-disk clearing process is more effective in the inner regions.

*Subject headings:* circumstellar matter – infrared: stars – planetary systems: formation

### 1. INTRODUCTION

From various lines of evidence (e.g., theoretical modeling, the cratering record on the Moon, returned Lunar samples, and isotopic data) it is believed that embryo terrestrial planets in the Solar System formed in  $\sim 10\text{--}30$  Myr, evolved through a period of potentially immense collisions, and then underwent a reduced, but still significant collisional period that ended with another violent episode – the Late Heavy Bombardment – at about 700 Myr (Kleine et al. 2002; Chambers 2004; Gomes et al. 2005; Strom et al. 2005). Thereafter, the system was in a relatively settled state, setting the stage for life to emerge on Earth. We are unsure whether this sequence was typical or exceptional. We are not even sure of the details of the steps because much of the evidence has been obliterated over time. Hard evidence must often be supplemented with relatively poorly tested theory to assemble a complete picture. The obvious solution would be to observe these processes as they are occurring in other planetary systems. However, observing terrestrial planets around nearby stars passing through parallel stages of evolution is virtually impossible. The planets are too dim for detection against the glare of the central stars; they are not sufficiently massive to be detected through gravitational recoil; and relatively few young stars lie close to the Sun.

However, there is a promising alternative approach, to study planetary debris disks. Debris disks arise from collisions of asteroidal (or planetesimal) bodies that lead to cascades of collisions among the resulting debris. Eventually, significant amounts of this material are ground down to dust grains. Because the surface area per unit mass is large for dusty material, when these grains are heated by the central star they can produce a readily detectable level of excess emission in the mid- and far-infrared. The behavior of these infrared excesses can trace the different zones within a planetary system. For grains around an A-type star and large enough to be in pseudo-stable orbits, the mid-IR band (*Spitzer* 24  $\mu\text{m}$ , *IRAS* and *ISO* 25  $\mu\text{m}$  passbands) is sensitive to material largely between  $\leq 5$  and  $\sim 50$  AU, while the far-IR band (*IRAS* and *ISO* 60  $\mu\text{m}$  and *Spitzer* 70  $\mu\text{m}$  passbands) is sensitive to material between  $\sim 50$  and 200 AU. Detailed studies of the behavior with age of debris disks in these two bands can indicate how the stages deduced for the early evolution of the Solar System are playing out in hundreds of other planetary systems.

Pioneering studies with *IRAS* and *ISO* suggest a systematic drop in infrared excess with stellar age (e.g., Habing et al. 2001; Spangler et al. 2001), qualitatively similar to the drop that would be deduced from the settling down of the Solar System. However, because of limitations in the sensitivity and the accuracy of measurements with these two missions, they were unable to show unambiguously how debris disks evolve. *Spitzer* brings significant advances in both sensitivity and photometric accuracy, increasing our ability to detect low levels of infrared excesses around hundreds of stars. A-type stars provide an ideal laboratory to study the early stages in planetary system evolution, particularly in the zones relevant for evolution of terrestrial planets (Earth-like tem-

<sup>1</sup> Steward Observatory, University of Arizona, 933 N Cherry Ave., Tucson, AZ 85721; ksu@as.arizona.edu

<sup>2</sup> JPL/Caltech, 4800 Oak Grove Drive, Pasadena, CA 91109

<sup>3</sup> Michelson Science Center, California Institute of Technology, M/S 100-22, Pasadena, CA 91125

<sup>4</sup> Department of Astrophysical Sciences, Princeton University, Princeton, NJ 08540

<sup>5</sup> Space Science Institute, 4700 Walnut St. Suit 205, Boulder, Colorado 80301

peratures occur at about 5 AU from such stars). Their main sequence lifetimes are long enough ( $\sim 800$  Myr) to encompass the entire period of interest, they are of high enough luminosity to light up their debris well, they are sufficiently abundant and bright that many can be observed readily, and they are cool enough that they are unlikely to create infrared excesses in the form of ionized gas. Rieke et al. (2005) have already conducted a study of the  $24/25 \mu\text{m}$  excesses in such stars, based on a combination of *IRAS* and Multiband Imaging Photometer for *Spitzer* (MIPS) measurements of stars in the field and MIPS measurements of stars in clusters. At that time, relatively few field stars had been measured well with *Spitzer* at  $70 \mu\text{m}$ . In this paper, we report MIPS photometry at 24 and  $70 \mu\text{m}$  of 160 main-sequence early type stars, enough to give a much better understanding of the evolution of debris systems.

## 2. OBSERVATIONS AND DATA REDUCTION

### 2.1. Sample Selection

The majority (128) of the stars in this study are from the *Spitzer* Guaranteed Time Observation (GTO) programs (Astar, Fab4, and Dirty12), where most of them were selected to have known ages based on cluster membership or association with moving groups. An additional 32 stars are included from the *Spitzer* calibration observations. In total, our sample includes 160 stars ranging in spectral type from B6 to A7, but mostly ( $\sim 85\%$ ) from B9 to A7. We have also developed a tool to determine ages from the Hertzsprung-Russell diagram (HRD) (Rieke et al. 2005) for consistency checking and estimating ages for the stars that are not in clusters or moving group associations. Two stars in the calibration programs are too bright to be observed at  $24 \mu\text{m}$ , while only 9 stars are bright enough at  $70 \mu\text{m}$  to be observed as calibrators. Hence, a total of 158 MIPS  $24 \mu\text{m}$  measurements and 137 MIPS  $70 \mu\text{m}$  measurements are reported here. The AOR keys, stellar properties and estimated ages are listed in Table 1.

Most of the stars in our sample are single stars (according to the literature and/or SIMBAD database); there are only 10 binary/multiple systems. These are either spectroscopic binaries (unresolved in ground-based optical photometry) or wide binaries with separations larger than the MIPS  $24 \mu\text{m}$  beam (resolved at  $24 \mu\text{m}$ ). In addition, we also double checked the stars with infrared excesses (identified by the method discussed below) in the 2MASS catalog, and found no nearby objects on the sky that could confuse the MIPS 24 and  $70 \mu\text{m}$  measurements. Therefore, the false detection of infrared excesses due to binary components or positional coincidence is unlikely.

### 2.2. Data Reduction and Source Extraction

All data were processed using the MIPS instrument team Data Analysis Tool (Gordon et al. 2005) for basic reduction (dark subtraction, flat fielding/illumination correction). The known transient behaviors associated with the Ge detectors were removed by time filtering the data in the  $70 \mu\text{m}$  default-scale mode, and by subtracting the off-source chopped background observations for data in the  $70 \mu\text{m}$  fine-scale mode. The processed data were then combined using the World Coordinate System

(WCS) information to produce final mosaics with pixels half the size of the physical pixel scale.

The photometry for each target was extracted using aperture photometry with multiple aperture settings as well as point-spread-function (PSF) fitting at both bands. By averaging the photometry using different methods (including multiple apertures), the estimated error provides a better estimate of the effects of image quality, background noise, and nearby contaminating sources. For aperture photometry at  $24 \mu\text{m}$ , we first determined the centroid of each target by fitting a 2-D Gaussian core, then computed the averaged integrated flux within a large aperture (a radius of  $14''.94$  with sky annulus between  $29''.88$  and  $42''.33$ ), and a small aperture (a radius of  $6''.23$  with sky annulus between  $19''.92$  and  $29''.88$ ). Because the PSF at  $70 \mu\text{m}$  is not well-sampled and the *Spitzer* pointing is good to within  $1''$ , for aperture photometry at  $70 \mu\text{m}$  default scale we used the WCS information to place the aperture center and measured total flux for two different aperture settings: a large aperture (a radius of  $29''.55$  with sky annulus between  $39''.40$  and  $68''.95$ ) and a small aperture (a radius of  $15''.96$  with sky annulus between  $18''.03$  and  $39''.01$ ). At  $70 \mu\text{m}$  fine-scale mode, we determined the centroid the same way as for the  $24 \mu\text{m}$  data, but only used a single aperture (a radius of  $16''$  with sky annulus between  $19''$  and  $39''$ ) due to the limited field of view. We determined the aperture correction based on the theoretical STinyTim PSFs (Krist 2002) that were smoothed to match the observed PSFs. An aperture correction of 1.143 (1.298) for the large aperture and 1.699 (1.972) for the small aperture was applied to the aperture photometry at  $24 \mu\text{m}$  ( $70 \mu\text{m}$  default-scale), respectively. A value of 1.933 for the  $70 \mu\text{m}$  fine-scale mode was used for the aperture correction.

We used, *StarFinder* (Diolaiti et al. 2000) to extract point-source photometry via PSF fitting. The PSF used at  $24 \mu\text{m}$  was constructed based on isolated calibration stars while at  $70 \mu\text{m}$  we used the smoothed STinyTim PSFs. For bright targets without other nearby contaminating sources, the results from aperture photometry and PSF fitting agree within 1% at  $24 \mu\text{m}$  and 2-5% at  $70 \mu\text{m}$ . Some stars in our sample are located in high cirrus regions; however, the background variation at  $70 \mu\text{m}$  is generally less than 10% across the whole field ( $5'$  by  $2.5'$ ). For the targets that have higher cirrus variations, we made sure that the extracted source position agrees within  $\lesssim 1''$  (a general *Spitzer* pointing error) between 24 and  $70 \mu\text{m}$ . The final measured flux and uncertainty were determined by averaging the different photometry methods. Conversion factors of  $1.05 \times 10^{-3}$ , 16.5, 61.6 mJy/arcsec<sup>2</sup> were used to transfer measured instrumental units to physical units (mJy) for  $24 \mu\text{m}$ ,  $70 \mu\text{m}$  default-, and fine-scale modes, respectively. The absolute flux calibration errors are less than 5% at  $24 \mu\text{m}$  and 10% at  $70 \mu\text{m}$  (Engelbracht et al. 2006, in preparation; Gordon et al. 2006, in preparation). The errors presented here are the intrinsic noise from images, and do not include the calibration errors.

At  $24 \mu\text{m}$ , the majority of the stars in the sample have high ( $\gg 20$ ) signal-to-noise detections, except those that have contamination from nearby back/foreground sources or nebulosity. For our  $70 \mu\text{m}$  observations, all stars observed in the GTO Astar program used the

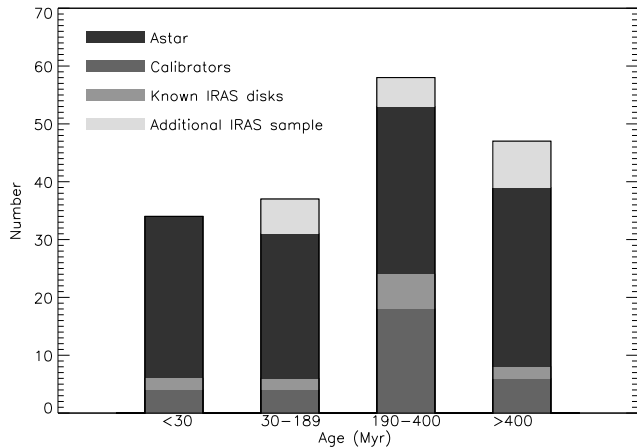


FIG. 1.— The age distribution of the complete sample.

default-scale photometry AOT. The integration times for these observations were planned to provide at least  $1\text{-}\sigma$  detection of the photosphere (including detector and background noises), but due to various circumstances of observations and general overestimations of the *Spitzer* sensitivity, many of these sources were not detected at  $70\ \mu\text{m}$ . Observations from the other GTO programs (Fab4 and Dirty12) targeted known *IRAS* debris disk candidates; therefore, the integration time was designed for high signal-to-noise detections. Finally, observations from the calibration program were aimed to detect the predicted photospheres at least at the  $3\text{-}\sigma$  level.

In all cases, a threshold of  $3\text{-}\sigma$  was set for source detection. If the signal-to-noise ratio is less than 3, we use the  $3\text{-}\sigma$  flux as an upper limit. We show in Table 1 the final measurements ( $F_{m,24}$  and  $F_{m,70}$  for 24 and  $70\ \mu\text{m}$ , respectively), uncertainties ( $\sigma_{24}$  and  $\sigma_{70}$ ) and signal-to-noise ratios ( $\text{SN}_{24}$  and  $\text{SN}_{70}$ ) for the entire sample.

### 2.3. Supplemental *IRAS* Sample

The stars observed with *Spitzer* were selected on the bases of (1) observability (background brightness and stellar magnitude) and (2) availability of accurate age estimates (membership in cluster or moving groups, etc.). There are a number of stars (47) that are logical members of our sample that have not been observed with *Spitzer* primarily because of the lack of accurate age estimates. Generally, the *Spitzer* programs emphasized young stars with ages from membership in moving groups or clusters, while these unobserved stars tend to be relatively old according to ages estimated from their placement on the HRD (Rieke et al. 2005). We added them to this study using *IRAS* data to avoid any age bias. To do so, we proceeded as follows.

Given the large *IRAS* beams, we were concerned that noise associated with the background might produce false excesses. The background (IR cirrus) can be estimated either directly from models of the infrared sky (e.g., from the *Spitzer* Science Center SPOT user tool) or from the atomic hydrogen column,  $n_{\text{H}}$  (e.g., Chandra Colden: Galactic Neutral Hydrogen Density Calculator<sup>6</sup>). We

used both methods to guard against stars in high cirrus regions; in general they gave consistent results. To determine a threshold for false excesses, we examined the  $K_s - [25]$  colors of the full sample of stars as a function of the two background estimators. We concluded that stars with  $n_{\text{H}} < 10\ \text{cm}^{-2}$  and IR background less than  $1.3\ \text{MJy/sr}$  at  $60\ \mu\text{m}$  are unlikely to suffer from cirrus confusion, and we trimmed the sample of 47 stars to 30 that meet both criteria. We next determined which of these stars have useful *IRAS* measurements at  $60\ \mu\text{m}$ . We used the Faint Source Catalog (FSC) to obtain a  $60\ \mu\text{m}$  flux density measurement and an error in the measurement for each star. Most of the stars are not detected, but the errors allow setting upper limits to their fluxes. We trimmed the sample to the 19 stars where there are either detected excesses, or we could set  $2\text{-}\sigma$  upper limits to the excesses at less than 5 times the photospheric flux density (Adopting  $2\text{-}\sigma$  limits allows meaningful limits in the same range as the *Spitzer* measurements, with a chance of one or two excesses slightly exceeding the actual limits for those 19 stars). Because the two cuts are based on sky properties, and then on *IRAS* signal to noise, the remaining stars should be representative of the original sample of twice as many. The properties of these 19 stars are listed in Table 2. The age distribution of the complete sample is shown in Figure 1.

## 3. PHOTOSPHERIC PREDICTION AND EXCESS DETERMINATION

### 3.1. Excess Identifications and Statistics

To determine the excess emission from the debris, the stellar contribution has to be subtracted from the measurements. We determined the stellar contribution at each band using the best-fit synthetic Kurucz model (Castelli & Kurucz 2003) by fitting all available optical to near infrared photometry (Johnson *UBVR IJHK* photometry, Strömgen *uvby* photometry, Hipparcos Tyco *BV* photometry, 2MASS *JHK<sub>s</sub>* photometry) based on a  $\chi^2$  goodness of fit test. For stars within 50 pc of the Sun, no correction for interstellar extinction was applied. For stars with distances larger than 50 pc, we estimated the extinction ( $A_V$ ) based on the  $B - V$  color and spectral type, and then applied a reddening correction using the extinction curve from Cardelli et al. (1989). The predicted flux was then computed using the best-fit Kurucz model spectrum at the 24 and  $70\ \mu\text{m}$  weighted average wavelengths ( $23.68$  and  $71.42\ \mu\text{m}$ , respectively).

To determine whether a star possesses a significant infrared excess, we first need to evaluate how good our photospheric predictions and measured photometry are. Figure 2 shows a histogram of the  $24\ \mu\text{m}$  fluxes ratioed to the expected photospheric values. A Gaussian distribution with a dispersion of 0.026 is shown for comparison, indicating our predicted photospheres and measured photometry are as good as 2.6% at the  $1\text{-}\sigma$  level. A few outliers of low flux ratio values are probably due to the effects of latent images (Engelbracht et al. 2006, in preparation). Note that the center of the Gaussian is at 0.981, suggesting a systematic offset of  $\sim 2\%$ . Based on this we define a  $3\text{-}\sigma$  excess as a ratio greater than 1.06 or a  $5\text{-}\sigma$  excess as a ratio greater than 1.11. There are four stars (HD 2266, HD 27045, HD 106591, and HD 74956) that have ratios between  $3\text{-}$  and  $5\text{-}\sigma$ , and three of them have confirmed  $70\ \mu\text{m}$  excesses (see below). Therefore,

<sup>6</sup> <http://cxc.harvard.edu/toolkit/colden.jsp>

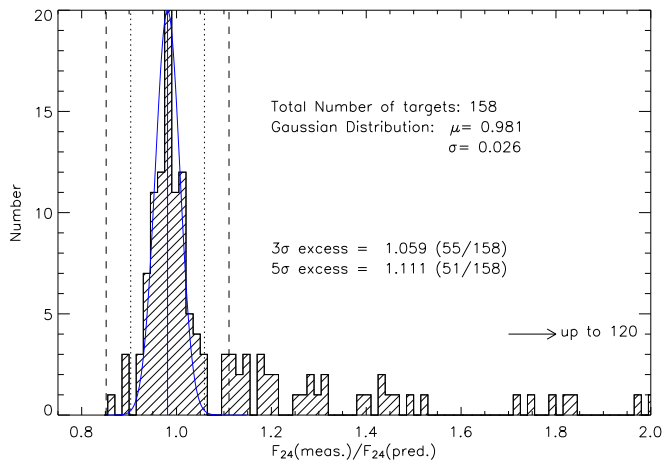


FIG. 2.— Distribution of the 24  $\mu\text{m}$  fluxes relative to the expected photospheric values from Kurucz model fittings. A Gaussian distribution with a dispersion of 0.026 is shown for comparison. Boundaries for  $\pm 3\sigma$  (dotted lines) and  $\pm 5\sigma$  (dashed lines) are marked.

we adopt the ratio of 1.06 ( $3\text{-}\sigma$  excess) as our threshold to identify infrared excesses at 24  $\mu\text{m}$ .

A total of 137 stars have MIPS 70  $\mu\text{m}$  observations, but only 69 stars have positive detections (signal-to-noise larger than 3). Figure 3 shows a histogram of the 70  $\mu\text{m}$  fluxes relative to the expected photospheric values. A Gaussian distribution with a dispersion of 0.15 and centered at 1.11 is shown for comparison. The majority of the stars (40 out of 69) show large excesses ( $>10\text{-}\sigma$ ). We define a  $3\text{-}\sigma$  excess as a ratio between measured and predicted fluxes greater than 1.55, and a  $5\text{-}\sigma$  excess as a ratio greater than 1.84 at 70  $\mu\text{m}$ . Four stars have ratios that fall between 3- and 5- $\sigma$  excesses; and three of them (HD 19356, HD 106591, HD 115892) have 24  $\mu\text{m}$  excess above  $3\text{-}\sigma$  (the exception is HD 4150). The  $3\text{-}\sigma$  threshold at 70  $\mu\text{m}$  is a consistent cutoff with the  $3\text{-}\sigma$  threshold at 24  $\mu\text{m}$  because none of the stars (a total of 22) that have ratios less than our  $3\text{-}\sigma$  threshold at 70  $\mu\text{m}$  has a 24  $\mu\text{m}$  excess (more than  $3\text{-}\sigma$ ).

Using these criteria ( $3\text{-}\sigma$  excess as a flux ratio higher than 1.06 at 24  $\mu\text{m}$  and 1.55 at 70  $\mu\text{m}$ ), each of the stars is then classified as “YES”, “NO” or “UPL” in Table 1 corresponding to having an infrared excess, being detected but with no excess above the  $3\text{-}\sigma$  confidence level, or only an upper limit. In addition, we also used the significance ( $\mathcal{X}$ ) of a detected excess, defined as (measured–predicted)/uncertainty, for an internal check. At 70  $\mu\text{m}$ , the excess stars identified by our flux ratio criterion all have  $\mathcal{X}_{70} \geq 3$ . At 24  $\mu\text{m}$ , two stars (HD 93738 and HD 137919) have the excess significance  $\mathcal{X}_{24}$  less than 3 while the rest all have  $\mathcal{X}_{24} \geq 3$ . Unfortunately, the 70  $\mu\text{m}$  measurements of these two stars are both upper limits, and cannot verify the infrared excess nature of these two stars. We, therefore, disregard HD 93738 and HD 137919 as having 24  $\mu\text{m}$  excesses. At the  $3\text{-}\sigma$  confidence level, the 24  $\mu\text{m}$  excess rate is  $32 \pm 5\%$  out of 155 stars (three stars are not debris disks in nature, see Sec 4.1). If we assumed that all the non-detected stars do not have 70  $\mu\text{m}$  excesses, then the 70  $\mu\text{m}$  excess rate is  $33 \pm 5\%$  (out of 134). This is a lower limit since in some cases the measured noise is much higher than the

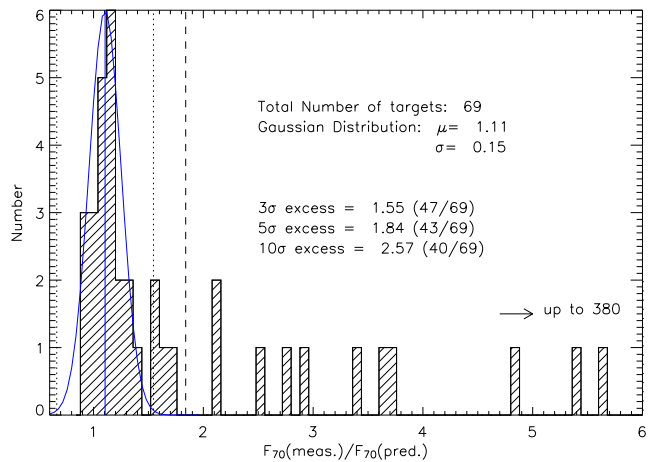


FIG. 3.— Distribution of the 70  $\mu\text{m}$  fluxes relative to the expected photospheric values from Kurucz model fittings. A Gaussian distribution with a dispersion of 0.15 is shown for comparison. Boundaries for  $\pm 3\sigma$  (dotted lines) and  $\pm 5\sigma$  (dashed lines) are marked.

predicted photospheric flux. Therefore the excess rate at 70  $\mu\text{m}$  could be as high as  $67 \pm 10\%$  (out of 66). Among the 44 stars that have excesses at 70  $\mu\text{m}$  above the  $3\text{-}\sigma$  confidence level, eight of them show no (less than  $3\sigma$ ) 24  $\mu\text{m}$  excess. These eight only-70 $\mu\text{m}$  excesses are unlikely to be false detections because the significance of the detected excesses are all greater than 4 at 70  $\mu\text{m}$  (See Table 3, group II).

The fact that the excess rate at 24  $\mu\text{m}$  and the lower-bound excess rate at 70  $\mu\text{m}$  are similar indicates that MIPS 24  $\mu\text{m}$  photometry is a very powerful and reliable tool to study infrared excesses around early-type stars. Combining both 24 and 70  $\mu\text{m}$  results, the infrared excess detection rate is at least  $37 \pm 5\%$  (58 out of 157) around A-type stars. Even using the same criteria ( $R_{24} > \sim 1.2$  and  $R_{70} > \sim 1.5$ ) for identifying excesses for the field (old) FGK stars ( $12 \pm 4\%$ , Bryden et al. 2006) and M-type stars ( $\sim 0\%$ , Gautier et al. 2006), the excess detection rate around A-type stars ( $\sim 30\%$ , using the same thresholds) is considerably higher.

### 3.2. Decay Times

The distributions of 24 and 70  $\mu\text{m}$  excesses with stellar age are illustrated in Figures 4 and 5. Twelve nearby debris disk stars discovered by *IRAS* are indicated by star-shaped symbols (for  $\beta$  Pic, Vega and Fomalhaut) and plus signs (for HD 14055, HD 18978, HD 38678, HD 74956, HD 95418, HD 102647, HD 139006, HD 161868, HD 181296). As has been found in Rieke et al. (2005), the amount of excess emission at 24  $\mu\text{m}$  shows a rapid decline with stellar age ( $\sim t_o/t$  and  $t_o \sim 150$  Myr), and a large variety of excess amounts at any given age. The trend at 70  $\mu\text{m}$  also shows a large variety at any given age in Figure 5. However, compared to the trend at 24  $\mu\text{m}$ , the 70  $\mu\text{m}$  excess trend has a much longer decay time with  $t_o \geq 400$  Myr.

We have carried out a simple analysis to show that the trends for different decay times at 24 and 70  $\mu\text{m}$  evident in Figures 4 and 5 are statistically significant. We divided the sample into two parts, based on the 24  $\mu\text{m}$  decay time scale of  $\sim 150$  Myr (Rieke et al. 2005). Given the

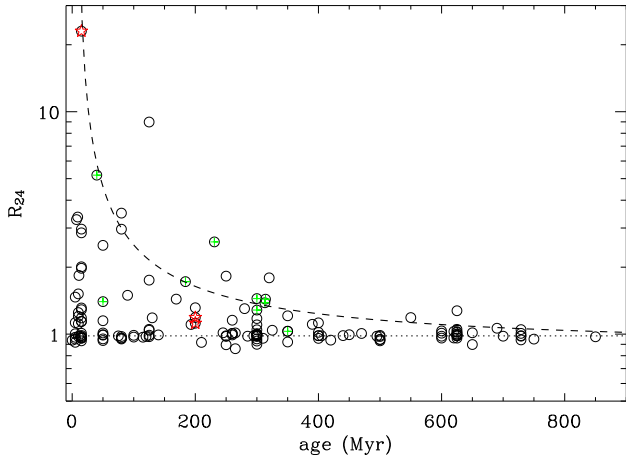


FIG. 4.— 24  $\mu\text{m}$  excess vs. age. Excess emission is indicated as the ratio of the observed flux density to that expected from the stellar photospheric value.  $\beta$  Pic, Vega and Fomalhaut are additionally marked as star-shaped symbols while stars from the *IRAS* discovered debris disks are shown as plus signs. A decay curve of  $t_o/t$  is indicated as the dashed line with  $t_o \sim 150$  Myr.

age uncertainties, we put the division at 400 Myr. For the stars with ages less than this value, we determined that the proportion of stars with excess ratios  $>1.3$  at 24  $\mu\text{m}$  and  $>5$  at 70  $\mu\text{m}$  were virtually identical (that is, 28 out of 109 and 26 out of 95, respectively). However, for the stars 400 Myr old or older, there were 0 stars out of 45 with excess ratios  $>1.3$  at 24  $\mu\text{m}$ , but 4 stars out of 38 with excess ratios  $>5$  at 70  $\mu\text{m}$ . We used the binomial theorem to show that the probability of these two results coming from the same parent distribution is only about 1%. That is, the 24  $\mu\text{m}$  excesses decay more rapidly than those at 70  $\mu\text{m}$  at the 99% confidence level.

#### 4. DUST PROPERTIES AROUND A STAR DEBRIS DISKS

##### 4.1. Circumstellar Gas Disks

Two stars in our sample, HD 21362 and HD58715, are associated with the Be phenomenon, i.e., where the strong stellar wind from a fast rotating B-type star forms a circumstellar gas disk, showing hydrogen emission lines in the optical and excess radiation relative to the expected photospheric flux in the infrared. The infrared excess emission is due to the free-free radiation from the ionized stellar wind. The nature of these gas disks can be recognized by several hydrogen lines seen in the IRS low resolution spectra (Figure 6). The spectra were observed as part of the GTO follow-up debris disk programs. Details of the observations and data reduction will be discussed in an upcoming paper (Su et al. 2006, in preparation).

These two stars as well as HD 58467 (a Herbig Ae/Be star) are not debris disks in nature, and are disregarded in the following discussion as well as the preceding discussion on the infrared excess rates.

##### 4.2. [24]–[70] Color temperature

In the following sections, we discuss the dust properties in terms of the observed [24]–[70] color temperature and fractional dust luminosity with stellar age. There are 36 stars that have both 24 and 70  $\mu\text{m}$  excesses, above  $3\text{-}\sigma$  confidence; hereafter we refer to them as group I.

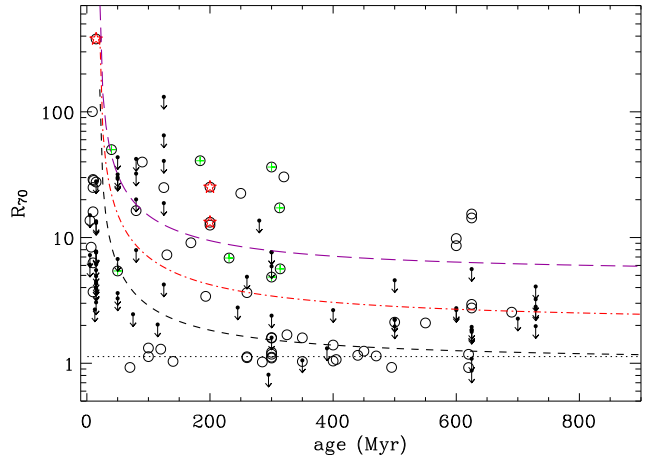


FIG. 5.— Similar to Figure 4 but for 70  $\mu\text{m}$  excess vs. age. The upper limits are shown in small dots with downward arrows. Three decay curves of  $t_o/t$  are indicated as the dashed line for  $t_o \sim 150$  Myr, the dot-dashed line for  $t_o \sim 400$  Myr, and the long-dashed line for  $t_o \sim 800$  Myr.

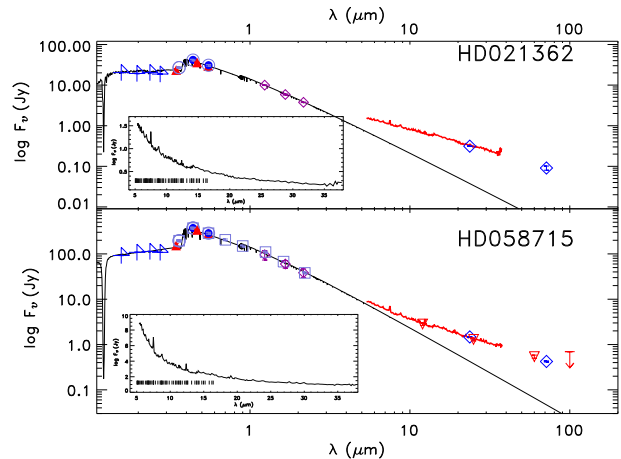


FIG. 6.— Spectral Energy Distributions for Be stars HD 21362 and HD 58715. Data plotted are: TD1 UV fluxes (plus signs), *uvby* photometry (filled triangles), Johnson UB (large open circles), Hipparcos photometry (small filled circles), 2MASS photometry (open diamonds), IRAS color corrected fluxes (downward triangles or downward arrows for upper limits), MIPS fluxes (open blue diamonds). The IRS spectra are shown in red lines between 5 and 38  $\mu\text{m}$ , as well as the small insets in a linear scale. The wavelengths of the hydrogen lines between 5 and 17  $\mu\text{m}$  are identified in the small inset. The prominent line at 7.495  $\mu\text{m}$  is the HI 18-8 line.

The stars that only show 70  $\mu\text{m}$  excess (a total of 8), we refer to as group II. Stars that have detections with  $S/N > 3$  at both 24 and 70  $\mu\text{m}$  but have no excess above the  $3\sigma$  levels, we refer to as group III (a total of 20). The infrared excess fluxes ( $F_{ire,24}$  and  $F_{ire,70}$  for 24 and 70  $\mu\text{m}$ , respectively), significance of the excess fluxes ( $\chi_{24}$  and  $\chi_{70}$ ), and the dust properties for stars from group I to III are listed in Table 3. Stars that have no significant 24  $\mu\text{m}$  excesses and for which the 70  $\mu\text{m}$  measurements are upper limits, we refer to as group IV (a total of 55). Group V (a total of 13) are the stars that have significant 24  $\mu\text{m}$  excesses (above  $3\text{-}\sigma$  confidence levels) but their 70  $\mu\text{m}$  measurements are upper limits.

One simple way to characterize the disk properties based on the 24 and 70  $\mu\text{m}$  excess emission is a blackbody

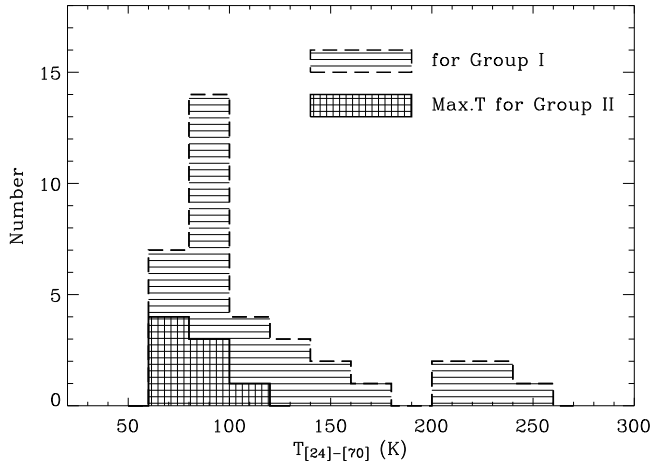


FIG. 7.— The  $[24 - 70]$  color temperature distribution of the disks. The stars that have both 24 and 70  $\mu\text{m}$  excesses (group I) are displayed in a horizontal-lined pattern. The maximum color temperatures for stars in group II (only 70  $\mu\text{m}$  excess) are shown in a mesh pattern.

fit to determine the color temperature ( $T_{[24]-[70]}$ ) of the disk. It is straightforward to determine the color temperature for group I stars by ratioing the flux density at the two bands. Including the uncertainty in the excess fluxes, the color temperature generally has an uncertainty of  $\pm 5$  K for the group I stars. For the stars in group II (excess at 70  $\mu\text{m}$  but not at 24  $\mu\text{m}$ ), a color temperature is computed by assuming that the excess flux at 24  $\mu\text{m}$  is three times the measured uncertainty, which serves as a maximum temperature that the dust can have, consistent with our photometric accuracy. Figure 7 shows the color temperature histogram for the group I and group II stars.

The majority of the debris disks have  $T_{[24]-[70]} \sim 90$  K, i.e., they are at a distance of  $\sim 100$  AU from the star if we assume that the dust particles in these systems are blackbody-like. The Kuiper belt in these A stars is expected to extend about 1.6 times farther than the Sun’s (45-55 AU) following a simple mass scaling (Su et al. 2005). Hence, most of the debris around these A stars is Kuiper-Belt-like if it consists of large (radius  $\geq 50$   $\mu\text{m}$ ) blackbody radiators. However, based on the study of the Vega debris disk (Su et al. 2005), non-blackbody-like small grains (radius  $\leq 10$   $\mu\text{m}$ ) can dominate the disk radiometric properties; therefore, the disk size can extend a few times larger if the dust grains in the system are small.

There are five stars that have  $[24]-[70]$  color temperatures larger than 200 K: HD 19356, HD 23862, HD 38678, HD 75416, and HD 115892. Since both HD 21362 and HD 58715 (gas disks) also have  $[24]-[70]$  color temperatures larger than 200 K, it is possible that these 5 stars are gas disks as well. However, no gas lines were seen in the mid-infrared spectra of HD 19356, HD 38678, and HD 115892 (Chen et al. 2006; Su et al. 2006, in preparation), which leaves only HD 23862 and HD 75416 as possible gas disks.

Figure 8 shows the distribution of the observed  $[24]-[70]$  color temperature with stellar age. Slightly smaller, but filled symbols represent the stars with ages determined from cluster associations. The ages deter-

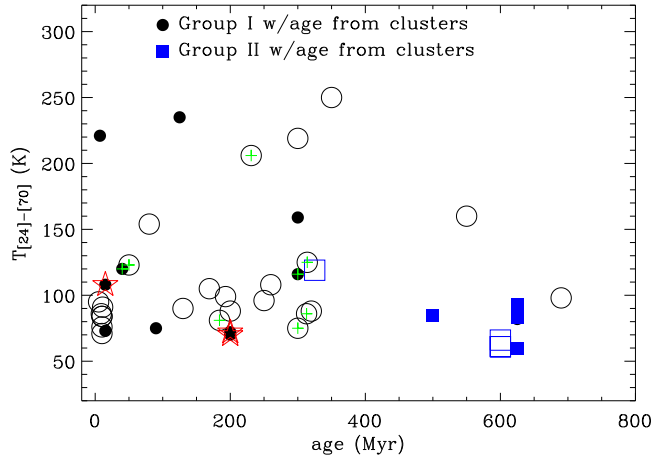


FIG. 8.— Stellar age vs. observed  $[24]-[70]$  color temperature. Symbols used are circles for stars that have both 24 and 70  $\mu\text{m}$  excess (group I), squares for stars only show 70  $\mu\text{m}$  excess (group II). Filled and smaller-size symbols are for stars with age associated with clusters or moving groups.  $\beta$  Pic, Vega and Fomalhaut are additionally marked as star-shape symbols while the stars from other IRAS discovered disks as plus signs.

mined from clusters or moving group association generally have errors less than 50%, but the ages determined from the HRD could have errors up to a factor of two. It appears that the color temperature of the disks has a slightly broader distribution when stars are younger. For stars older than 400 Myr, most of the color temperatures of the disks appear in a narrow range between 50-150 K. Assuming the dust we see is blackbody-like (i.e., the location of the dust is directly related to dust temperature and stellar properties), the decrease of the  $[24]-[70]$  color suggests that the debris is located further away from the stars in the older systems, consistent with the significant difference in decay time scales between 24 and 70  $\mu\text{m}$ , found in Sec 3.2.

#### 4.3. Trends in Amounts of Excess Emission

Since the amounts of excess at both 24 and 70  $\mu\text{m}$  decrease with stellar age (shown in Sec 3.2), it is important to have a large number of stars especially in the old age bin to ensure good statistics. As stated in Sec 2.3, an additional 19 A-type stars with *IRAS* observations at 25 and 60  $\mu\text{m}$  were included to avoid an age bias. There are two candidates among these stars to show possible excesses at 25  $\mu\text{m}$ : HD 56537, with a flux ratio of 1.32, and HD 79469 with a flux ratio of 1.30. Both are in the “marginal” category, since the deviations from unity flux ratio (no excess) are less than  $3\sigma$ . There is only one star with a well-detected excess at 60  $\mu\text{m}$ , HD 39014 (see, e.g., Jura et al. 2004). HD 142105 has a possible excess at 60  $\mu\text{m}$  ( $3.9\sigma$ ). For all the remaining stars, there are only upper limits at 60  $\mu\text{m}$ . To analyze all the stars in this sample and in our *Spitzer* sample, in the following we will discuss  $2\sigma$  upper limits for *IRAS* measurements at a uniform level of 1.25 at 25  $\mu\text{m}$  and 5 at 60  $\mu\text{m}$ .

These values correspond to a color temperature of  $\sim 90$  K, which is typical of most of the debris systems (see Figure 7). We divide stars from the *Spitzer* sample into those with measured excesses above these limits, or excess or upper limits below them (i.e.,  $R_{24} > 1.25$  and

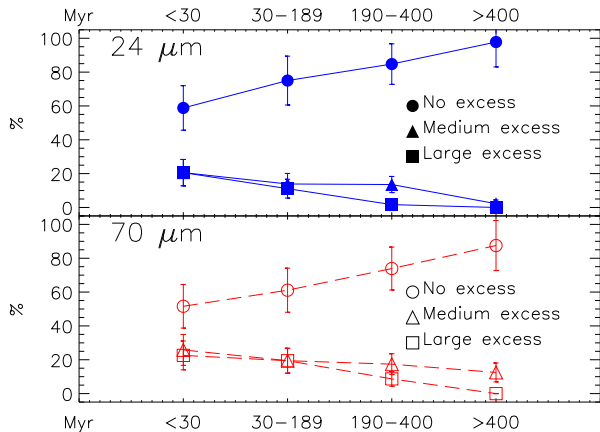


FIG. 9.— Trends of excesses with age at both 24 and 70  $\mu\text{m}$ , based on Table 1. The 24  $\mu\text{m}$  results are plotted as filled symbols with solid connecting lines while the 70  $\mu\text{m}$  results are as open symbols with dashed connecting lines. “No excess” is shown in circles, “Medium excess” in triangles, and “Large excess” in squares.

$R_{70} > 5$  even with the 2- $\sigma$  upper limits). Combining the *IRAS* and *Spitzer* samples, a total of 174 stars were used at 24/25  $\mu\text{m}$ , and 153 stars for 60/70  $\mu\text{m}$  to study the trends in amounts of excess emission.

We further group the observations into bins in ages and amount of excess for three subgroups: “no” means no excess; “large” means a flux ratio greater than 2 for 24  $\mu\text{m}$  and 20 for 70  $\mu\text{m}$ ; “medium” means the flux ratio is intermediate. The age bins were set so that the total number of stars in each age bin is roughly equal. The results are shown in Table 4 and Figure 9. The 24  $\mu\text{m}$  excess trend is consistent with the results of Rieke et al. (2005) that  $\sim 50\text{--}60\%$  of the stars that are younger than 30 Myr have no 24  $\mu\text{m}$  excess, rising to  $\sim 85\text{--}95\%$  for the stars that are older than 190 Myr. The trend of no excess at 70  $\mu\text{m}$  is similar to 24  $\mu\text{m}$  within the errors, but with a systematically lower fraction.

The trends of infrared excess (either medium or large) are, again, similar, but the fractions at 70  $\mu\text{m}$  are systematically higher than at 24  $\mu\text{m}$ , suggesting that the rate of 70  $\mu\text{m}$  excesses is higher than at 24  $\mu\text{m}$  and the persistence time of the 70  $\mu\text{m}$  excess is longer; i.e., the debris primarily emitting at 70  $\mu\text{m}$  remains in the system longer.

#### 4.4. Fractional Dust Luminosity

The most frequently used quantity to measure the amount of dust in these systems is the fractional luminosity,  $f_d$ : the ratio of the total emission by dust to the stellar luminosity ( $f_d = L_{IR}/L_*$ ). It measures the fraction of the sky seen from the star that is covered by dust, and therefore the fraction of the stellar radiation that will be absorbed and re-emitted in the infrared (Dominik & Decin 2003). The fractional luminosity can be determined based on the observed [24]–[70] color temperature and an assumption of blackbody emission for the dust. However, the fractional luminosity estimated in this way is somewhat over-estimated since the dust grains in the system probably have a  $\lambda^{-\beta}$  emissivity dependence where  $\beta = 1\text{--}2$ , and emit less efficiently at longer wavelengths than blackbody emission. The overestimate

TABLE 4  
EXCESS AMOUNT V.S. AGE

Myr	tot#	No	Medium	Large
for 24/25 $\mu\text{m}$				
$t \leq 30$	34	20(58%)	7(21%)	7(21%)
$30 < t \leq 189$	36	27(75%)	5(13%)	4(11%)
$190 < t \leq 400$	59	50(85%)	8(14%)	1(2%)
$400 < t$	45	44(98%)	1(2%)	0(0%)
for 60/70 $\mu\text{m}$				
$t \leq 30$	31	16(52%)	8(25%)	7(23%)
$30 < t \leq 189$	36	22(62%)	7(19%)	7(19%)
$190 < t \leq 400$	46	34(74%)	8(17%)	4(9%)
$400 < t$	40	35(88%)	5(12%)	0(0%)

REFERENCES. — Definitions of “No”, “Medium Excess” and “Large Excess” for flux ratio at 24  $\mu\text{m}$  ( $R_{24/25}$ ) and 70  $\mu\text{m}$  ( $R_{60/70}$ ) are: no –  $R_{24} < 1.25$ ; large –  $R_{24} > 2$ ; median –  $1.25 \leq R_{24} \leq 2$ ; no –  $R_{70} < 5$ ; large –  $R_{70} > 20$ ; median –  $5 \leq R_{70} \leq 20$ .

could be large, depending on details of the emissivity law. We discuss HD 225200 as an example in Sec 4.5; the fractional luminosity is  $\sim 8\%$  over-estimated between a blackbody and modified blackbody emission.

Large errors will result if these disks have substantial emission from cold ( $\sim 30$  K) dust. In most cases, there are no observations to constrain this possibility very well. However, examining the three best-studied nearby A-type debris disks, Vega, Fomalhaut and  $\beta$  Pic, we find the flux ratio between 70 and 850  $\mu\text{m}$  is  $\sim 140$ ,  $\sim 92$ , and  $\sim 125$ , respectively. Given the distinctly different properties of these three disks (age, fractional luminosity, and disk extent), an average flux ratio of  $\sim 120$  between 70 and 850  $\mu\text{m}$  should be representative for early-type debris disks. This average flux ratio gives a dust temperature of  $\sim 64$  K assuming a  $\beta=1$  emissivity law, and the resultant fractional luminosity is roughly equal to or less than the one computed using the maximum color temperature. Applying similar logic, an upper-limit fractional luminosity is also estimated for each of the stars in group III using a computed color temperature by assuming that the excess flux at each band is three times the measured uncertainty.

A histogram of fractional luminosity is shown in Figure 10. The majority of the stars have a fractional infrared luminosity  $\sim 5 \times 10^{-5}$ . Stars that only show 70  $\mu\text{m}$  excess (group II) generally have lower fractional infrared luminosity. The maximum fractional luminosities for group III stars are much lower than the group I and II stars, consistent with their non-detectable infrared excess. To see the general trend of the fractional luminosity with age, we divide the group I and II stars into two age bins: older or younger than 300 Myr. This division is roughly at half the main sequence lifetime of an A0 V star (the histogram is not sensitive to this age; it is similar if we make the cut at an age of 400 Myr). The fractional luminosity distribution for these two age groups is shown in Figure 11; older stars tend to have lower fractional luminosity than younger ones, which confirms the results from Sec 3.2 and Figure 9.

The distribution of the fractional luminosity with stellar age is shown in Figure 12. Several characteristics are

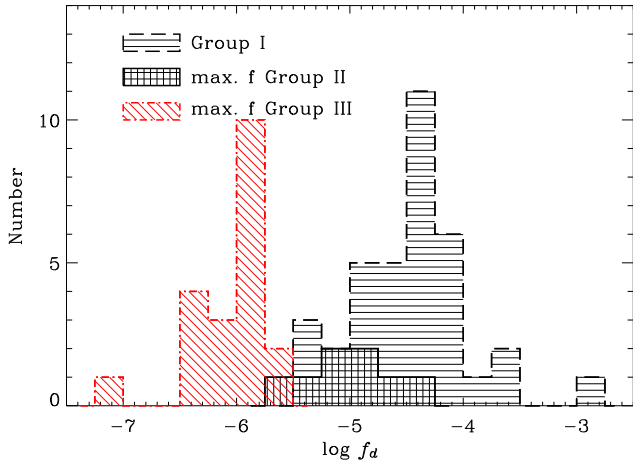


FIG. 10.— The fractional infrared luminosity distribution of the debris disks around A-type stars. The stars that have both 24 and 70  $\mu\text{m}$  excesses (group I) are displayed in horizontal-lined pattern while the stars in group II (70  $\mu\text{m}$  excess only) are in a mesh pattern. The group III distribution shows that our detection limits are strong enough that there should be no significant bias in the group I/II comparison.

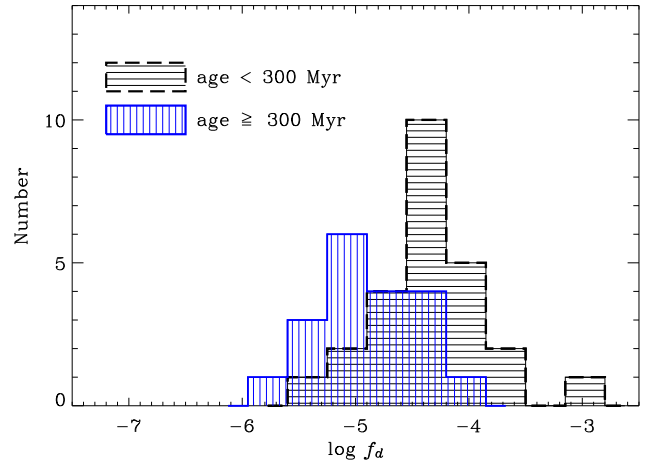


FIG. 11.— Same as Figure 10 but with two age bins (older or younger than 300 Myr) among the group I and II stars.

found in this  $f_d$  vs. age diagram:

1. The data are consistent with a general  $1/t$  relation in the  $f_d$  vs. age diagram but with at least two orders of magnitude variation in the amounts of  $f_d$ .
2. An upper envelope of  $1/t$  is seen in Figure 12. We do not detect any stars that are older than 100 Myr and have  $f_d$  values greater than  $10^{-3}$  in this early-type sample.
3. All the only-70 $\mu\text{m}$  excess stars (group II, squares in Figure 12) are old. No stars that are younger than 100 Myr have only-70  $\mu\text{m}$  excess. This trend could result from sample selection bias, because most of the young stars are at larger distances, and only 70  $\mu\text{m}$  upper limits were obtained. Among the 53 group IV stars (no 24  $\mu\text{m}$  excess and 70  $\mu\text{m}$  is an upper limit), 6 are younger than 100 Myr, have  $3\text{-}\sigma$  upper limit ratios larger than 5, and most importantly their backgrounds are clean based on the 24  $\mu\text{m}$  images. These 6 stars are potential only-70  $\mu\text{m}$  excess young stars. Future deeper 70  $\mu\text{m}$  observations can help to better identify their natures.
4. Stars that have no detectable excess (group III, upside down triangles with downward arrows in Figure 12) have  $f_d$  as low as  $\sim 10^{-7}$  (similar to the value in our Solar System).

A constant upper envelope of  $f_d \approx 10^{-3}$  is suggested by Decin et al. (2003) based on a re-analysis of the data obtained with ISOPHOT and revised age estimates. This upper constant cutoff is not seen in these new *Spitzer* observations (item 2). Although Decin et al. combine all the available spectral types on the same plot, it is possible that the maximum fractional luminosity is different for different spectral types.

Dominik & Decin (2003) suggest that the total disk mass in a system and the location and sizes of the parent bodies are the three major parameters in determining the place in the  $f_d$  vs. age diagram. They conclude that a  $1/t$  relation indicates the dust removal process is dominated by collisions, and that Pointing-Robertson (P-R) drag would yield a  $1/t^2$  relation. Collisions which result in small grains that are blown out of the system via radiation pressure are the dominant mechanism in removing dust in the bright debris disk systems observed by *IRAS* and *ISO*. This is true for these early-type stars since blowout occurs for grains  $\lesssim 10 \mu\text{m}$ ; however, radiation pressure from lower luminosity stars (late K and M dwarfs) may not be adequate to remove grains at all, and stellar wind drag is the dominant mechanism to remove grains in the young late K to M dwarfs (Plavchan et al. 2005). Hence, for the A - G systems, P-R drag only plays an important role when the density of the debris is as low as in our solar system (Dominik & Decin 2003; Wyatt 2005). Therefore, most (if not all) of the stars in the  $f_d$  vs. age diagram should follow a  $1/t$  trend. This is consistent with what we see in these new *Spitzer* data.

Assuming that the group IV stars have no 70  $\mu\text{m}$  excess as well, the true lower envelope in the  $f_d$  vs. age diagram is then very low. The total surface area occupied by dust may be greatly enhanced by collisions, and then follow a  $1/t$  steady state collisional cascade. If the only-70  $\mu\text{m}$  excesses are, indeed, only found associated with older stars, it means that the clearing process (collisions) is an inside-out process. The collision frequency is higher closer to the stars because of larger relative velocities; therefore, the dust will be ground down to finer debris (subject to radiation blowout) faster. This is consistent with what Wyatt (2005) has suggested.

Alternatively, the “clearing” of the inner region could also arise from the decline of inward grain transport, rather than the removal of the initial inner disk grain population. A secular decline in the collision rate in the outer disk might account for a drop in inward grain transport, and thus a drop in 24  $\mu\text{m}$  emission with time. A crucial question for this model is whether the particles generated at the 70  $\mu\text{m}$  emission zone (50-200 AU for A stars) have enough time to drift inward before they get



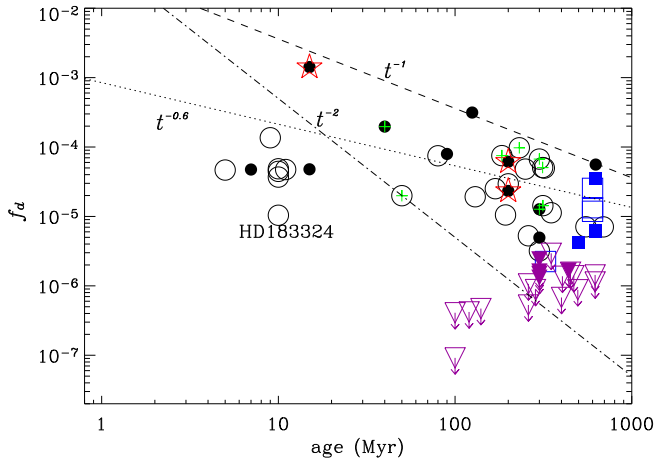


FIG. 12.— Stellar age vs. fractional luminosity. Symbols used are the same as Figure 8. Additional data points from group III stars (maximum detectable fractional luminosity) are shown as upside-down triangles with arrows pointing downward, indicating our detection limits. The  $1/t$  relation is shown as a dashed line while  $1/t^2$  as a dot-dashed line, with arbitrary normalization. A  $1/t^{0.6}$  relation was obtained by fitting all the confirmed excess stars (group I and II), shown as a dotted line.

destroyed by collisions. Assuming an A-type star of  $2.5 M_{\odot}$  and  $60 L_{\odot}$  with a debris disk of  $f_d \sim 5 \times 10^{-5}$ , the P-R lifetime ( $\sim 10^{7-8}$  yr) is roughly 100 times the collisional lifetime ( $\sim 10^{5-6}$  yr) for grains with radii  $\sim 100 \mu\text{m}$  and density of  $2.5 \text{ g/cm}^3$  at distances of 50-200 AU from the star. Therefore, the population of the particles that drift inward from the  $70 \mu\text{m}$  zone to the  $24 \mu\text{m}$  emission zone is likely to be small. Furthermore, we do not expect the color temperature to evolve with time if the  $24 \mu\text{m}$  emission comes from material that is spiraling in from the colder, outer disk via P-R drag. The amount of the dust we see in these systems suggests the dominant particle removal mechanism is through collisions. P-R drag may only be important for older systems because it does not explain the dust temperature trend seen in the systems from 5 to 850 Myr of age.

#### 4.5. Debris disk Model: Vega-like grains or KBO-like grains

As has been thoroughly discussed in the literature, debris disk modeling based on the broadband SED alone is degenerate, and hence not conclusive in constraining the debris distribution or dust properties. Based on the resolved disk surface brightness profiles (100-800 AU), Su et al. (2005) have shown that the majority of the dust particles in the disk are small grains in the proto-type Vega debris disk. In comparison, the Vega SED has been modeled using large 30-200  $\mu\text{m}$  grains in a ring-like (80-120 AU) disk (Dent et al. 2000). Resolving the disk extent is important. Unfortunately most of the debris disks we discuss here are not resolved with *Spitzer's* beams. Without further constraints, there are many degeneracies using two data points (24 and  $70 \mu\text{m}$ ) to constrain a (at least) 6-parameter disk model (surface density power-law index  $p$ , grain size power-law index  $q$ , grain size limits ( $a_{min}$  to  $a_{max}$ ), disk extent ( $R_{in}$  to  $R_{out}$ )).

As an illustration, we fit the observed SED of HD 225200 with two different pre-determined models: Vega-

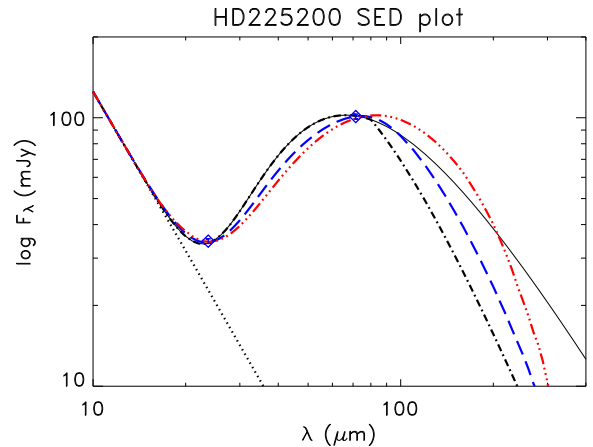


FIG. 13.— Model SEDs for HD 225200. The black dotted line represents the stellar photosphere. The black solid line is the SED assuming blackbody emission at  $T_d = 75 \text{ K}$  while the dash-dotted black line is assuming a modified blackbody emission  $(\frac{\lambda}{\lambda_o})^{-1} B_{\lambda}(75 \text{ K})$  with  $\lambda_o = 80 \mu\text{m}$ . The blue long dashed line is the best-fit SED using KBO-like grains while the red dash-triple-dotted line is the best-fit SED using Vega-like grains. Both models go through the 24 and  $70 \mu\text{m}$  points, but have noticeably different shapes between these points.

like or KBO-like, using astronomical silicate grains. In the Vega-like model, we restrict the grains to be “small” (i.e.,  $a_{min} \sim 1 \mu\text{m}$ ,  $a_{max} < 50 \mu\text{m}$ ,  $q = -2.5$ ), and to be driven outward by radiation pressure, therefore,  $p = 1$ . In the KBO-like model, we restrict the grains to be “large” (i.e.,  $a_{min} \sim 10 \mu\text{m}$ ,  $a_{max} = 100 \mu\text{m}$ ,  $q = -3.5$ ), and to spiral inward due to the P-R drag, therefore,  $p = 0$ . The remaining two parameters to fit are  $R_{in}$  and  $R_{out}$ .

We searched large regions of parameter space, computing a  $\chi^2$  statistic at each point. At 90% confidence, we find that  $R_{in} = 35 \pm 15 \text{ AU}$ ,  $R_{out} = 120 \pm 117 \text{ AU}$  with dust mass of  $8.5 \pm 4.3 \times 10^{-3} M_{\oplus}$  for the KBO-like model, and  $R_{in} = 100 \pm 55 \text{ AU}$ ,  $R_{out} = 900 \pm 450 \text{ AU}$  with dust mass of  $21.40 \pm 5.2 \times 10^{-3} M_{\oplus}$  for the Vega-like model. Figure 13 shows the resultant SEDs. The outer radius in the Vega-like model ( $\sim 900 \text{ AU}$ ,  $\sim 7''$  given a distance of 129 pc) is theoretically resolvable with MIPS at  $24 \mu\text{m}$ . The fact that our shallow  $24 \mu\text{m}$  observation indicates HD 225200 to be an unresolved point source indicates either that deeper imaging might be required to detect the disk outer boundary, or that Vega-like grains are not likely present in the system. Furthermore, the two models yield different amounts of emission at wavelengths greater than  $\sim 100 \mu\text{m}$ . Without resolved images, data points at far-infrared and sub-millimeter wavelengths can provide further constraints on the disk outer boundary. Follow-up IRS observations of these A-type debris disks can also put additional constraints on the disk model (inner radius and grain sizes), and will be addressed in another paper.

## 5. SUMMARY AND CONCLUSION

About 160 A-type main-sequence stars with ages ranging from 5 to 850 Myr were measured at 24 and/or  $70 \mu\text{m}$  using the Multiband Imaging Photometer for *Spitzer*. With *Spitzer's* unprecedented sensitivity, we are able to

identify infrared excesses of  $\sim 6\%$  at  $24\ \mu\text{m}$  and  $\sim 55\%$  at  $70\ \mu\text{m}$  above the photospheres at the  $3\text{-}\sigma$  levels. At this  $3\text{-}\sigma$  confidence level, the infrared excess rate is  $32\pm 5\%$  and  $\geq 33\pm 5\%$  for  $24$  and  $70\ \mu\text{m}$ , respectively. The excess detection rate around these early-type stars is significantly higher than the one found in the old FGK (Bryden et al. 2006) and M-type stars (Gautier et al. 2006). However, recent studies by Gorlova et al. (2006) and Siegler et al. (2006) show that the excess rate for young FGK stars is also higher than for old FGK stars; most importantly, the evolution in the trend of excess rate vs. age looks similar between A stars and FGK stars (only the absolute fraction is different) in their studies. It is difficult to determine whether there is an intrinsic difference in the infrared excess rates between A-type and FGK stars because equivalent levels of fractional luminosity become increasingly hard to detect as the star becomes cooler. The incidence of debris disks is actually the convolution of how many stars actually possess debris disks with given properties, and how detectable the disks are with *Spitzer*, and this convolution is a strong function of spectral type. Thus debris-disk excess emission is not a steep function of stellar type. Since the detectability of a given level of fractional excess decreases with decreasing stellar temperature, the incidence of excesses is consistent with a similar debris disk driven fractional excesses between A and K stars. Nevertheless, it appears that age is the most important factor in determining the detectability of infrared excess among A- to K-type main-sequence stars, not stellar mass.

The amount of excess emission decreases with stellar age and follows a simple  $t_o/t$  relationship in general with  $t_o \sim 150$  Myr for excesses at  $24\ \mu\text{m}$  but  $t_o \geq 400$  Myr at  $70\ \mu\text{m}$ ; that is,  $24\ \mu\text{m}$  excesses decay more rapidly than those at  $70\ \mu\text{m}$ . In addition, at any given age there exists a large variety in the amount of  $24$  and  $70\ \mu\text{m}$  ex-

cess emission. The observed  $[24]-[70]$  color temperatures for a total of 44 debris disks with  $24$  and/or  $70\ \mu\text{m}$  excesses range from  $\sim 60$  to  $\sim 250$  K, but the majority of the disks have a typical temperature of  $\sim 90$  K. Furthermore, older stars (age  $> 300$  Myr) tend to have colder observed  $[24]-[70]$  color temperatures than young ones. Assuming the dust we detect is blackbody-like, the decline of the  $[24]-[70]$  color implies the debris is located further away from the stars in the older systems.

The fractional luminosity for these 44 early-type debris disks ranges from  $\sim 10^{-3}$  to  $\sim 10^{-6}$ . The trend between the fractional luminosity and stellar age follows a general  $1/t$  relationship; older stars tend to have lower fractional luminosity than younger ones. An upper envelope of  $1/t$  is seen in the fractional luminosity vs. age diagram, suggesting that collisions followed by radiation pressure blowing out small grains are the dominant process to remove grains in these systems. The decreases of observed  $[24]-[70]$  color temperatures and the fractional luminosity suggest that the debris disk clearing is an inside-out process.

Based on observations with NASA *Spitzer* Space Telescope, which is operated by the Jet Propulsion Laboratory, California Institute of Technology under NASA contract 1407. Support for this work was provided by NASA through Contract Number 1255094 issued by JPL/Caltech. This research made use of the SIMBAD database, operated at CDS, Strasbourg, France. This publication makes use of data products from the Two Micron All Sky Survey, which is a joint project of the University of Massachusetts and the Infrared Processing and Analysis Center/California Institute of Technology, funded by the National Aeronautics and Space Administration and the National Science Foundation.

## REFERENCES

- Barrado y Navascués, D. 1998, *A&A*, 339, 831  
 Bonatto, C., Bica, E., & Girardi, L. 2004, *A&A*, 415, 571  
 Bryden, G., et al. 2006, *ApJ*, 636, 1098  
 Cardelli, J. A., Clayton, G. C., & Mathis, J. S. 1989, *ApJ*, 345, 245  
 Castelli, F., & Kurucz, R. L. 2003, *IAU Symposium*, 210, 20P  
 Chambers, J. E. 2004, *Earth and Planetary Science Letters*, 223, 241  
 Chen, C. H., et al. 2006, *ArXiv Astrophysics e-prints*, arXiv:astro-ph/0605277 (*ApJS*, in press.)  
 Corbally, C. J. 1984, *ApJ*, 285, 195  
 Corbally, C. J., & Gray, R. O. 1996, *AJ*, 112, 2286  
 Decin, G., Dominik, C., Waters, L. B. F. M., & Waelkens, C. 2003, *ApJ*, 598, 636  
 Dent, W. R. F., Walker, H. J., Holland, W. S., & Greaves, J. S. 2000, *MNRAS*, 314, 702  
 de Zeeuw, P. T., Hoogerwerf, R., de Bruijne, J. H. J., Brown, A. G. A., & Blaauw, A. 1999, *AJ*, 117, 354  
 Diolaiti, E., Bendinelli, O., Bonaccini, D., Close, L., Currie, D., & Parmeggiani, G. 2000, *A&AS*, 147, 335  
 Dominik, C., & Decin, G. 2003, *ApJ*, 598, 626  
 Eggen, O. J. 1983, *AJ*, 88, 642  
 Gautier, T. N. III, Rieke, G. H. Stansberry, J. A., Bryden, G. C., Stapelfeldt, K. R., Werner, M. W., Beichman, C. A., Chen, C. H., Su, K. Y. L., Trilling, D., Patten, B., & Roellig, T. 2006, submitted.  
 Gerbaldi, M., Faraggiana, R., Burnage, R., Delmas, F., Gómez, A. E., & Grenier, S. 1999, *A&AS*, 137, 273  
 Gomes, R., Levison, H. F., Tsiganis, K., & Morbidelli, A. 2005, *Nature*, 435, 466  
 Gordon, K. D., et al. 2005, *PASP*, 117, 503  
 Gorlova, N., et al. 2006, *ApJ*, in press.  
 Habing, H. J., et al. 2001, *A&A*, 365, 545  
 Iliev, I. K., & Barzova, I. S. 1995, *A&A*, 302, 735  
 Jura, M., et al. 2004, *ApJS*, 154, 453  
 King, J. R., Villarreal, A. R., Soderblom, D. R., Gulliver, A. F., & Adelman, S. J. 2003, *AJ*, 125, 1980  
 Kleine, T., Munker, C., Mezger, K., & Palme, H. 2002, *Nature*, 418, 952  
 Krist, J. 2002, *TinyTim/SIRTF User's Guide*, version 1.3.  
 Lynga, G., & Wramdemark, S. 1984, *A&A*, 132, 58  
 Mamajek, E. E., Lawson, W. A., & Feigelson, E. D. 2000, *ApJ*, 544, 356  
 Odenkirchen, M., Soubiran, C., & Colin, J. 1998, *New Astronomy*, 3, 583  
 Panagi, P. M., & O'dell, M. A. 1997, *A&AS*, 121, 213  
 Paunzen, E. 1997, *A&A*, 326, L29  
 Perryman, M. A. C., et al. 1998, *A&A*, 331, 81  
 Plavchan, P., Jura, M., & Lipsy, S. J. 2005, *ApJ*, 631, 1161  
 Randich, S., Pallavicini, R., Meola, G., Stauffer, J. R., & Balachandran, S. C. 2001, *A&A*, 372, 862  
 Rieke, G. H., et al. 2004, *ApJS*, 154, 25  
 Rieke, G. H., et al. 2005, *ApJ*, 620, 1010  
 Siegler, N., Muzerolle, J., Young, E. T., Rieke, G. H., Mamajek, E. E., Trilling, D. E., Gorlova, N., & Su, K. Y. L., 2006, submitted.  
 Song, I., Caillault, J.-P., Barrado y Navascués, D., Stauffer, J. R., & Randich, S. 2000, *ApJ*, 533, L41  
 Song, I., Caillault, J.-P., Barrado y Navascués, D., & Stauffer, J. R. 2001, *ApJ*, 546, 352  
 Spangler, C., Sargent, A. I., Silverstone, M. D., Becklin, E. E., & Zuckerman, B. 2001, *ApJ*, 555, 932  
 Strom, R. G., Malhotra, R., Ito, T., Yoshida, F., & Kring, D. A. 2005, *Science*, 309, 1847

Su, K. Y. L., et al. 2005, ApJ, 628, 487

Westin, T. N. G. 1985, A&AS, 60, 99

Wyatt, M. C. 2005, A&A, 433, 1007

Zuckerman, B., Song, I., & Webb, R. A. 2001, ApJ, 559, 388

Zuckerman, B., & Song, I. 2004, ARA&A, 42, 685

TABLE 1  
SAMPLE OF STARS AND MIPS MEASUREMENTS

Name	AOR Key	SpType	distance pc	Cluster/ Moving Group	Age Myr	Age ref.	$F_{m,24}$ mJy	$\sigma_{24}$ mJy	SN <sub>24</sub>	R <sub>24</sub>	IRE <sub>24</sub>	$F_{m,70}$ mJy	$\sigma_{70}$ mJy	SN <sub>70</sub>	R <sub>70</sub>	IRE <sub>70</sub>
HD000319	3972864	A1V	80.3	...	600	3	43.69	0.78	56.01	0.979	NO	<13.6	4.53	3	2.742	UPL
HD001160	10090496	A0V	136.6	...	0 <sup>b</sup>	22	10.56	0.2	52.8	0.939	NO	...	...	...	...	...
HD002262	3692544	A7V	23.5	...	690	22	304.61	4.05	75.21	1.063	YES	78.7	3.74	21.04	2.548	YES
	6036736															
	3692544															
	6036736															
HD002811	9940224	A3V	205.8	...	750	22	10.56	0.07	150.86	0.95	NO	...	...	...	...	...
HD004150	3973120	A0IV	73.7	...	325	4	139.99	2.5	56	1.041	NO	24.73	2.23	11.09	1.685	YES
HD011413	3973376	A1V	74.8	...	600	3	50.73	0.91	55.75	1.034	NO	52.32	2.15	24.33	9.817	YES
HD011636	4228096	A5V	18.3	...	620	5	811.52	3.28	247.41	0.961	NO	85.76	9.38	9.14	0.924	NO
HD014055	8796416	A1Vnn	36.1	...	300	6	282.66	6.63	42.63	1.445	YES	787.83	157.57	5	36.377	YES
	8796160															
HD014228	9021952	B8IV/V	47.5	...	115	5	185.6	1.66	111.81	0.969	NO	<41.23	13.74	3	2.033	UPL
HD014943	9940480	A5V	61.3	...	850	22	47.35	0.47	100.74	0.973	NO	...	...	...	...	...
HD015004	3973632	A0III	198.0	...	280	4	31.33	0.31	101.06	1.302	YES	<35.88	11.96	3	13.64	UPL
HD015008	7345408	A1.5V	41.5	...	405	5	178.77	1.44	124.15	0.983	NO	21.13	0.44	48.02	1.07	NO
HD015646	3973888	A0V	118.1	...	260	4	19.59	0.2	97.95	1.008	NO	<10.25	3.42	3	4.875	UPL
HD016970	3974144	A3V	25.1	Ursa Major	300	7	353.27	3.06	115.45	1.046	NO	45.29	4.75	9.53	1.223	NO
HD017254	11783424	A2V	124.1	...	650	22	29.24	0.45	64.98	0.898	NO	...	...	...	...	...
HD018978	8794368	A4V	26.4	...	350	5	240.39	2.63	91.4	1.03	NO	<26.56	8.86	3	1.054	UPL
	8794112															
HD019356	3974656	B8V	28.5	...	300	8,5	1404.88	6.84	205.39	1.175	YES	206.23	11.79	17.49	1.586	YES
HD020315	3975168	B8V	197.6	$\alpha$ Per	80	8	37.46	10.66	3.51	0.951	NO	<135.93	45.31	3	32.257	UPL
HD020888	11783680	A3V	58.0	...	300	22	36.06	0.73	49.4	0.9	NO	...	...	...	...	...
HD021362 <sup>‡</sup>	3976192	B6Vn	169.8	$\alpha$ Per	80	8	313.31	3.66	85.6	8.201	YES	90.93	5.74	15.84	22.25	YES
HD021551	3976448	B8V	266.7	$\alpha$ Per	80	8	27.61	1.04	26.55	0.958	NO	<61.37	20.46	3	20.103	UPL
HD021981	8812544	A1V	113.5	...	265	5	39.15	0.8	48.94	0.86	NO	...	...	...	...	...
HD023267	3976960	A0V	136.4	$\alpha$ Per	80	8	35.55	0.42	84.64	2.964	YES	<55.72	18.57	3	42.209	UPL
HD023642	3977984	A0V	110.4	Pleiades	125	8	17.3	1.68	10.3	1.041	NO	<237.24	79.08	3	131.549	UPL
HD023753	3978240	B8V	103.7	Pleiades	125	8	39.88	2.53	15.75	0.989	NO	<83.47	27.82	3	18.786	UPL
HD023763	3978496	A1V	144.9	Pleiades	125	8	18.75	1.91	9.82	1.051	NO	<128.04	42.68	3	64.946	UPL
HD023862	3978752	B8IVevar	118.8	Pleiades	125	8	662.14	6.4	103.46	8.986	YES	202.43	23.37	8.66	24.965	YES
HD023923	3979264	B8V	116.6	Pleiades	125	8	46.21	0.89	51.92	1.749	YES	<118.80	39.6	3	40.679	UPL
HD023964	3975936	A0V	158.7	Pleiades	125	8	17.15	0.25	68.6	0.974	NO	<8.00	2.67	3	4.23	UPL
HD025860	15421440	A4.5IV	132.8	...	400	22	26.26	0.1	262.6	0.984	NO	...	...	...	...	...
HD026321	3979520	A0V	175.1	$\alpha$ Per	80	8	13.48	0.11	122.55	0.976	NO	<12.2	4.07	3	7.945	UPL
HD027045	3979776	A3m	28.7	...	193	8,5	133.49	0.87	153.44	1.105	YES	45.73	7.03	6.5	3.406	YES
HD027628	3980032	A3m	45.7	Hyades	625	9	71.59	0.61	117.36	1.001	NO	<14.60	4.87	3	1.832	UPL
HD027749	3980288	A1m	47.2	Hyades	625	9	71.68	0.58	123.59	0.982	NO	<14.39	4.8	3	1.778	UPL
HD027962	3980544	A2IV	45.4	Hyades	625	9,5	149.06	2.75	54.2	0.96	NO	<96.41	32.14	3	5.61	UPL
HD028226	3980800	Am	48.0	Hyades	625	9	72.96	1.02	71.53	1.051	NO	107.55	10.11	10.64	14.311	YES
HD028355	3981056	A7V	49.2	Hyades	625	9,5	137.19	1.1	124.72	1.274	YES	178.78	5.45	32.8	15.389	YES
HD028527	3981312	A6IV	44.4	Hyades	625	9,5	120.07	1.52	78.99	1.019	NO	37.36	5.94	3.83	2.94	YES
HD028546	3981568	Am	44.3	Hyades	625	9	75.31	0.46	163.72	1.026	NO	<15.38	5.13	3	1.947	UPL
HD029388	3981824	A6V	45.9	Hyades	625	9,5	183.72	1.28	143.53	0.985	NO	<21.88	7.29	3	1.087	UPL
HD029488	3982080	A5Vn	48.8	Hyades	625	9	139.51	0.51	273.55	0.987	NO	<13.36	4.45	3	0.875	UPL
HD030210	3982336	Am	81.7	Hyades	625	9	70.33	0.73	96.34	0.986	NO	<14.19	4.72	3.01	1.85	UPL
HD030422	3982592	A3IV	57.5	...	10	3,5	44.67	0.64	69.8	1.202	YES	64.52	1.01	63.88	16.024	YES

TABLE 1  
SAMPLE OF STARS AND MIPS MEASUREMENTS – CONTINUE.

Name	AOR Key	SpType	distance pc	Cluster/ Moving Group	Age Myr	Age ref.	$F_{m,24}$ mJy	$\sigma_{24}$ mJy	SN <sub>24</sub>	R <sub>24</sub>	IRE <sub>24</sub>	$F_{m,70}$ mJy	$\sigma_{70}$ mJy	SN <sub>70</sub>	R <sub>70</sub>	IRE <sub>70</sub>
HD031295	3982848	A0V	37.0	...	10	3,5	167.25	1.94	86.21	1.25	YES	418.72	4.64	90.24	28.952	YES
HD033254	3983104	A2m	53.9	Hyades	625	9	72.62	1.39	52.24	1	NO	21.46	2.17	9.89	2.752	YES
HD034868	3983360	A0V	136.8	...	300	4	25.9	0.3	86.33	0.983	NO	<21.68	7.23	3	7.658	UPL
HD038056	3983616	A0V	132.5	...	250	4,5	36.48	0.37	98.59	1.823	YES	49.67	1.06	46.86	22.466	YES
HD038206	3983872	A0V	69.2	...	9	4	106.92	1.58	67.67	3.361	YES	342.27	12.87	26.59	100.367	YES
HD038545	3984128	A3Vn	129.5	...	13	4	45.89	0.72	63.74	0.979	NO	<13.6	4.53	3	2.678	UPL
HD038678	8792832	A2Vann	21.5	...	231	8,5	860.2	17.2	50.01	2.598	YES	246.62	24.66	10	6.872	YES
	9798208															
HD039060	8970240	A5V	19.3	$\beta$ Pic	12	23,1,2	7276	728	9.99	23.015	YES	12990.4	1825.4	7.12	379.678	YES
	12613632															
HD040335	9192192	A0	112.7	...	5	5	18.11	0.48	37.73	0.919	NO	...	...	...	...	...
HD042525	13588224	A0V	101.8	...	300	22	33.39	0.32	104.34	0.976	NO	...	...	...	...	...
HD043107	13476608	B8V	84.9	...	80	5	56.18	1.1	51.07	0.961	NO	...	...	...	...	...
HD045557	3984640	A0V	88.0	...	75	4	35.82	0.31	115.55	0.982	NO	<9.54	3.18	3	2.454	UPL
HD046190	9662976	A0V	79.0	...	5	5	23.86	0.05	477.2	1.126	YES	...	...	...	...	...
HD047332	11892224	A1IV	343.6	...	400	22	16.41	0.28	58.61	1.019	NO	...	...	...	...	...
HD048915	9458432	A0V	2.6	...	70	8,5	...	...	...	...	...	2535.26	17.81	142.35	0.926	NO
HD057336	13588736	A0IV	384.6	...	400	10	10.05	0.18	55.83	0.957	NO	...	...	...	...	...
HD058142	7145472	A1V	76.3	...	250	22	97.27	0.76	127.99	0.896	NO	...	...	...	...	...
HD058647 <sup>†</sup>	3985152	B9IV	277.0	...	1	Ae/Be	2163.32	10.55	205.05	118.166	YES	267.78	3.03	88.38	131.912	YES
HD058715 <sup>‡</sup>	3985408	B8Ve	52.2	...	100	22,6	1469.42	7.75	189.6	3.413	YES	423.04	51.02	8.29	8.91	YES
HD065517	13589248	A2.5IV	105.9	...	350	22	14.76	0.22	67.09	1.031	NO	...	...	...	...	...
HD069863	13589504	A2V	74.2	...	650	5,11	81.78	3.6	22.72	1.014	NO	...	...	...	...	...
HD071043	3985664	A0V	73.1	...	11	4	58.21	1.44	40.42	1.836	YES	97.22	29.12	3.34	28.442	YES
HD071155	3985920	A0V	38.3	...	169	8,5	302.39	4.13	73.22	1.437	YES	211.74	2.76	76.72	9.087	YES
HD073210	3986432	A5V	196.1	Praesepe	729	12	24.7	0.2	123.5	1.048	NO	<10.66	3.55	3	4.078	UPL
HD073666	3986688	A1V	174.8	Praesepe	729	12	16.6	0.83	20	0.979	NO	<5.26	1.75	3.01	2.818	UPL
HD073731	3986944	A5m	168.1	Praesepe	729	12	30.05	0.51	58.92	0.942	NO	<6.78	2.26	3	1.973	UPL
HD073819	3987200	A6Vn	183.2	Praesepe	729	12	21.03	0.19	110.68	1.008	NO	<6.13	2.04	3	2.732	UPL
HD073871	3987456	A0III	160.5	Praesepe	729	12	19.26	0.09	214	0.984	NO	<6.76	2.25	3	3.231	UPL
HD074956	8794880	A1V	24.4	...	390	8,5	1396.18	25.37	55.03	1.107	YES	<180.08	60.03	3	1.315	UPL
	8794624															
HD075416	3987712	B8V	96.9	$\eta$ Cha	8	23,13,14	122.44	1.29	94.91	3.273	YES	34.5	0.93	37.1	8.381	YES
HD076644	4239360	A7V	14.6	...	620	5	629.55	4.1	153.55	1.028	NO	78.54	2.28	34.45	1.178	NO
HD079108	3987968	A0V	115.2	...	320	4	44.98	1.16	38.78	1.791	YES	84.35	2.52	33.47	30.357	YES
HD080007	10091008	A2IV	34.1	...	260	5	1768.9	4.54	389.63	1.006	NO	212.86	0.97	219.44	1.126	NO
HD080950	3988224	A0V	80.8	...	80	4	114.67	1.53	74.95	3.5	YES	59.31	0.96	61.78	16.361	YES
HD082621	12398336	A2V	81.9	...	285	5	127.75	0.85	150.29	0.979	NO	14.51	0.71	20.44	1.024	NO
HD083808	4231680	A5V	41.5	...	400	5	816.76	1.28	638.09	0.984	NO	94.79	1.49	63.62	1.041	NO
HD087887	3988480	A0III	88.1	...	295	4	108.94	0.27	403.48	0.983	NO	<9.81	3.27	3	0.811	UPL
HD087901	9661440	B7V	23.8	...	140	5	1591.5	6.57	242.24	0.992	NO	179.25	35.85	5	1.034	NO
HD091375	9663232	A1V	79.4	...	265	5	102.48	2.1	48.8	1.013	NO	...	...	...	...	...
HD092467	3988992	B9.5V	141.2	IC2602	50	15	13.32	1.4	9.51	0.994	NO	<46.44	15.48	3	31.787	UPL
HD092536	3989248	B8V	147.1	IC2602	50	15	46.19	0.55	83.98	2.507	YES	<60.76	20.25	3	30.078	UPL

TABLE 1  
SAMPLE OF STARS AND MIPS MEASUREMENTS – CONTINUE.

Name	AOR Key	SpType	distance pc	Cluster/ Moving Group	Age Myr	Age ref.	$F_{m,24}$ mJy	$\sigma_{24}$ mJy	SN <sub>24</sub>	R <sub>24</sub>	IRE <sub>24</sub>	$F_{m,70}$ mJy	$\sigma_{70}$ mJy	SN <sub>70</sub>	R <sub>70</sub>	IRE <sub>70</sub>
HD092715	3989504	B9.5V	130.7	IC2602	50	15	12.76	0.45	28.36	1.012	NO	<40.78	13.59	3	29.305	UPL
HD092783	3989760	B9V	138.7	IC2602	50	15	13.39	0.37	36.19	0.99	NO	<64.45	21.48	3	43.523	UPL
HD092845	3990016	A0V	185.5	...	300	4	40.64	0.84	48.38	0.952	NO	<11.05	3.68	3	2.392	UPL
HD093540	3990272	B6V	143.1	IC2602	50	15	40.04	0.6	66.73	0.952	NO	<16.35	5.45	3	3.615	UPL
HD093549	3990528	B7IV	131.6	IC2602	50	15	44.95	1.12	40.13	0.936	NO	<17.2	5.73	3	3.277	UPL
HD093738	3990784	B9.5V	143.9	IC2602	50	15	23.87	1.38	17.3	1.149	NO <sup>#</sup>	<15.51	5.17	3	6.748	UPL
HD095418	7596800	A1V	24.3	Ursa Major	300	7,8,5	1026.6	14.14	72.6	1.283	YES	421.13	84.23	5	4.849	YES
	7596288															
HD097585	3991040	A0V	146.2	...	300	4	50.65	2.98	17	0.931	NO	<35.55	11.85	3	5.904	UPL
HD097633	3991296	A2V	54.5	...	550	5	395.1	2.48	159.31	1.187	YES	75.17	1.88	39.98	2.092	YES
HD101452	15247104	A2	128.2	...	250	22	13.05	0.12	108.75	0.977	NO	...	...	...	...	...
HD102647	4314112	A3V	11.1	...	50	8,5	1599.68	14.68	108.97	1.4	YES	676.47	45.54	14.85	5.421	YES
	4313856															
HD103287	3991552	A0V	25.6	Ursa Major	300	7,8,5	788.49	7.37	106.99	0.987	NO	96.06	1.73	55.53	1.118	NO
HD105805	3991808	A4Vn	94.3	Coma	500	16	38.09	0.46	82.8	0.947	NO	<8.69	2.9	3	1.963	UPL
HD106591	3992064	A3V	25.0	Ursa Major	300	7,5	419.18	4.13	101.5	1.101	YES	65.45	3.79	17.27	1.601	YES
HD108382	3992320	A4V	86.5	Coma	500	16	113.99	0.99	115.14	0.987	NO	26.87	1.23	21.85	2.122	YES
HD108767	3992576	B9.5V	26.9	...	260	5	412.69	2.44	169.14	0.992	NO	49.26	1.9	25.93	1.107	NO
HD108945	3992832	A2pvar	95.3	Coma	500	16	55.18	0.92	59.98	0.976	NO	<27.78	9.26	3	4.574	UPL
HD109307	3993088	A4Vm	106.3	Coma	500	16	26.69	0.51	52.33	0.933	NO	<6.98	2.33	3	2.235	UPL
HD110304	8811008	A1IV	40.0	...	400	5,11	...	...	...	...	...	144.58	8.6	16.81	1.396	NO
HD110411	3993344	A0V	36.9	...	10	3	139.88	1.21	115.6	1.517	YES	247.95	2.22	111.69	25.002	YES
HD111786	3993600	A0III	60.2	...	200	3	66.01	1.1	60.01	1.314	YES	69.86	3.65	19.14	12.55	YES
HD112185	3993856	A0p	24.8	Ursa Major	300	7,5	1457.98	13.41	108.72	0.99	NO	178.35	4.2	42.46	1.1	NO
HD112413	3994112	A0spe	33.8	...	350	5	337.05	7.84	42.99	0.922	NO	40.27	1.75	23.01	1.032	NO
HD115892	3994368	A2V	18.0	...	350	5	683.66	2.41	283.68	1.209	YES	96.62	6.47	14.93	1.593	YES
HD116706	3994624	A3IV	78.0	Coma	500	16	40.88	0.65	62.89	0.945	NO	<10.25	3.42	3	2.211	UPL
HD116842	3714304	A6Vn	24.9	Ursa Major	300	7	258.68	1.47	175.97	0.985	NO	33.42	3.68	9.08	1.156	NO
HD118878	3994880	A0V	121.2	Upper Cen	15	14	20.19	0.33	61.18	0.96	NO	<7.01	2.34	3	3.051	UPL
HD123445	3995136	B9V	218.8	UCen	15	14	18.96	0.54	35.11	0.963	NO	<12.91	4	3.23	6.14	UPL
HD125162	3995392	A0p	29.8	...	313	8,5	270.8	2.32	116.72	1.384	YES	364.67	3.88	93.99	17.225	YES
HD126135	3995648	B8V	155.5	Upper Cen	15	14	22.49	1.7	13.23	2.008	YES	<34.54	11.51	3	27.998	UPL
HD126997	3995904	A0.5V	144.5	Upper Cen	15	14	19.67	0.2	98.35	0.986	NO	<8.56	2.85	3	3.988	UPL
HD128207	3996160	B8V	128.5	Upper Cen	15	14	30.99	0.67	46.25	1.139	YES	<11.65	3.88	3	3.908	UPL
HD128998	15247360	A1V	131.4	...	250	22	32.05	0.28	114.46	0.983	NO	...	...	...	...	...
HD129655	15421696	A2	128.5	...	300	22	16.53	0.12	137.75	0.999	NO	...	...	...	...	...
HD130697	3996416	A2V	128.2	Upper Cen	15	14	17.49	0.44	39.75	0.933	NO	<9.09	3.03	3	4.499	UPL
HD130841	6037760	A3IV	23.7	...	495	5	785.59	3.59	218.83	0.979	NO	81.9	3.08	26.59	0.927	NO
HD132238	3996672	B8V	191.9	Upper Cen	15	14	30.6	0.91	33.63	1.977	YES	<12.81	4.27	3	7.601	UPL
HD133880	3996928	B8IV...	126.6	Upper Cen	15	14	27.26	0.41	66.49	0.973	NO	<12.81	4.27	3	4.293	UPL
HD133937	3997184	B7V	136.2	Upper Cen	15	14	23.09	0.23	100.39	0.959	NO	<11.25	3.75	3	4.332	UPL
HD135454	3997440	B9V	137.2	Upper Cen	15	14	17.71	0.15	118.07	1.311	YES	<8.00	2.67	3	5.502	UPL
HD135742	3997696	B8V	49.1	...	100	8,5	501.99	1.68	298.8	0.988	NO	71.5	8.37	8.54	1.322	NO
HD136246	3997952	A1V	143.5	Upper Cen	15	14	14.93	0.22	67.86	1.288	YES	34.35	1.41	24.36	27.614	YES
HD136347	3998208	A0sp	123.5	Upper Cen	15	14	15.91	2.67	5.96	1.009	NO	<8.35	2.78	3	4.925	UPL

TABLE 1  
SAMPLE OF STARS AND MIPS MEASUREMENTS – CONTINUE.

Name	AOR Key	SpType	distance pc	Cluster/ Moving Group	Age Myr	Age ref.	$F_{m,24}$ mJy	$\sigma_{24}$ mJy	SN <sub>24</sub>	R <sub>24</sub>	IRE <sub>24</sub>	$F_{m,70}$ mJy	$\sigma_{70}$ mJy	SN <sub>70</sub>	R <sub>70</sub>	IRE <sub>70</sub>
HD136482	3998464	B8.5V	124.5	Upper Cen	15	14	42.11	0.3	140.37	2.966	YES	<20.91	6.97	3	13.485	UPL
HD137015	3998720	A2V	146.6	Upper Cen	15	14	15.18	0.26	58.38	1.183	YES	<18.01	6	3	13.068	UPL
HD137919	3998976	B9V	154.3	Upper Cen	15	14	21.04	6.1	3.45	1.141	NO <sup>‡</sup>	<15.31	5.1	3	7.76	UPL
HD138923	3999232	B8V	112.5	Upper Cen	15	14	58.05	0.37	156.89	2.854	YES	<17.21	5.74	3	7.675	UPL
HD139006	8793600	A0V	22.9	...	314	8,5	1261.63	15.46	81.61	1.436	YES	542.03	80.7	6.72	5.633	YES
	8793344															
HD139160	3999488	B9IV	184.2	Upper Sco	5	14	20.98	0.1	209.8	0.968	NO	<35.49	11.83	3	15.048	UPL
HD142703	3999744	A2Ib/II	52.9	...	300	17	54.27	0.39	139.15	0.988	NO	<46.51	15.5	3	7.63	UPL
HD144661	4000256	B8IV/V	117.6	Upper Sco	5	14	17.19	0.24	71.63	1.004	NO	<11.13	3.71	3	6.076	UPL
HD145964	4000768	B9V	105.8	Upper Sco	5	14	19.01	1.6	11.88	0.95	NO	<15.72	5.24	3	7.248	UPL
HD158460	7970048	A1V	104.4	...	260	5	53.15	0.34	156.32	1.155	YES	18.26	1.19	15.34	3.646	YES
HD158485	7969280	A4V	109.3	...	420	5	24	0.1	240	0.94	NO	...	...	...	...	...
HD161868	8797184	A0V	29.1	...	184	8,5	413.51	18.31	22.58	1.722	YES	1085.19	217	5	40.819	YES
	8796928															
HD163466	12872448	A2	196.5	...	310	5	20.15	0.13	155	0.958	NO	...	...	...	...	...
HD165459	9851392	A2V	89.3	...	5	5	25.32	0.25	101.28	1.467	YES	25.93	1.08	24.01	13.664	YES
HD172167	9547776	A0V	7.8	Castor	200	1,2	8900	89	100	1.12	YES	11416.1	2283.22	5	13.236	YE
	9458432															
HD172728	12872704	A0V	130.5	...	210	5	31.33	0.15	208.87	0.918	NO	...	...	...	...	...
HD181296	8935424	A0Vn	47.7	Tucana	30	23,18	382.43	6.46	59.2	5.186	YES	408.53	41.37	9.87	50.033	YES
	8935168															
HD183324	4002048	A0V	59.0	...	10	3	50.3	1.25	40.24	1.114	YES	30.76	4.89	6.29	6.29	YES
HD188228	3725824	A0V	32.5	...	10	8,5	170.75	0.55	310.45	0.977	NO	68.95	6.1	11.3	3.695	YES
HD193281	4002560	A2III	218.3	...	600	3	27.26	1.93	14.12	1.01	NO	<7.96	2.65	3	2.649	UPL
HD198160	4002816	A2.5IV/V	73.2	...	600	3	62.52	0.64	97.69	0.96	NO	62.07	5.78	10.74	8.609	YES
HD204041	4003328	A1IV	87.3	...	400	3	33.54	0.37	90.65	1.124	YES	<8.78	2.93	3	2.647	UPL
HD209952	7979008	B7IV	31.1	...	100	5	979.38	1.78	550.21	0.97	NO	120.77	0.71	170.1	1.129	NO
	7345152															
	9661696															
	13642240															
HD210049	3729920	A2V	40.0	...	245	5	128.47	0.38	338.08	1.014	NO	<37.84	12.61	3	2.775	UPL
HD210111	4003584	A2III/IV	78.7	...	700	3	36.59	1.25	29.27	0.979	NO	<9.46	3.15	3	2.264	UPL
HD210418	4003840	A2V	29.6	...	450	5	336.71	3.32	101.42	0.994	NO	46.82	3.48	13.45	1.248	NO
HD213320	4004096	A0IVs	81.4	...	300	4	71.85	0.85	84.53	1.005	NO	<12.24	4.08	3	1.6	UPL
HD214923	4004352	B8V	63.9	...	120	5	241.91	2	120.96	0.977	NO	34.62	1.51	22.93	1.295	NO
HD215789	4004608	A3V	39.7	...	470	5	363.17	2.37	153.24	1.007	NO	45.67	4.43	10.31	1.143	NO
HD216956	4889088	A3V	7.7	Castor	200	1,2	3850	190	20.26	1.188	YES	9057.11	736.4	12.3	25.189	YES
	12582400															
HD216627	4004864	A3V	48.9	Ursa Major	300	7,19	420.03	2.16	194.46	0.985	NO	54.7	7.12	7.68	1.18	NO
HD221756	4004608	A1III	71.6	...	130	3	62.46	1.08	57.83	1.184	YES	41.52	2.68	15.49	7.283	YES
HD225200	3972608	A0V	129.0	Blanco 1	90	20,21	34.7	0.7	49.57	1.495	YES	101.05	2.36	42.82	39.857	YES

REFERENCES. — 1: Barrado y Navascues (1998); 2: Song et al. (2000); 3: Paunzen (1997); 4: Gerbaldi et al. (1999); 5: Rieke et al. (2005); 6: Westin (1985); 7: King et al. (2003); 8: Song et al. (2001); 9: Perryman et al. (1998); 10: Corbally & Gray (1996); 11: Corbally (1984); 12: Bonatto et al. (2004); 13: Mamajek et al. (2000); 14: de Zeeuw et al. (1999); 15: Randich et al. (2001); 16: Odenkirchen et al. (1998); 17: Iliev & Barzova (1995); 18: Zuckerman et al. (2001); 19: Eggen (1983); 20: Panagi & O'dell (1997); 21: Lynga & Wramdemark (1984); 22: this study; 23: Zuckerman & Song (2004).

NOTE. — <sup>b</sup> Age is set to 0 for the young stars that are below the ZAMS on the HRD; <sup>†</sup> Herbig Ae/Be star; <sup>‡</sup> Be stars; <sup>‡</sup> stars are disregarded having 24  $\mu$ m excess due to  $\chi_{24} < 3$ .

TABLE 2  
 INFORMATION ON THE ADDITIONAL IRAS STARS

Name	2MASS $K_s$ mag	Age Myr	SpType	$F_{25}$ Jy	$R_{25}$	$F_{60}$ Jy	$R_{60}$	$\sigma_{R_{60}}$	$\mathcal{X}_{60}$	upper limit
HD050241	2.62	660	A7IV	0.891	0.993	0.230	1.48	0.31	1.54	2.10
HD005448	3.50	600	A5V	0.395	0.994	0.118	1.71	0.46	1.54	2.63
HD033904	3.61	150	B9IV	0.355	1.032	0.127	2.13	0.43	2.65	2.98
HD141003	3.31	300	A2IV	0.439	0.964	0.177	2.24	0.54	2.31	3.31
HD027376	3.91	160	B9V	0.247	0.947	0.103	2.27	0.52	2.44	3.32
HD130109	3.72	300	A0V	0.353	1.088	0.125	2.22	0.55	2.20	3.33
HD077327	3.42	120	A1Vne	0.478	1.165	0.161	2.26	0.56	2.23	3.39
HD080081	3.51	395	A3V	0.393	1.042	0.151	2.31	0.58	2.27	3.46
HD056537	3.38	560	A3V	0.586	1.320	0.177	2.30	0.60	2.17	3.49
HD118098	3.13	510	A3V	0.550	0.986	0.236	2.44	0.54	2.68	3.51
HD079469	3.93	180	B9.5V	0.332	1.296	0.109	2.45	0.61	2.37	3.68
HD153808	3.79	220	A0V	0.289	0.991	0.139	2.74	0.58	3.03	3.90
HD088955	3.73	300	A2V	0.356	1.154	0.148	2.76	0.77	2.28	4.31
HD198001	3.72	240	A1.5V	0.318	1.023	0.155	2.87	0.78	2.41	4.42
HD089021	3.37	410	A2IV	0.431	0.963	0.232	2.98	0.75	2.66	4.48
HD142105	4.12	180	A3Vn	0.247	1.147	0.125	3.34	0.60	3.89	4.55
HD129246	3.64	320	A3IVn	0.342	1.023	0.177	3.05	0.79	2.58	4.63
HD140436	3.77	160	B9IV+	0.237	0.793	0.171	3.30	0.73	3.17	4.75
HD039014	3.70	540	A7V	0.314	0.988	0.841	15.24	1.68	8.49	18.59

NOTE. — Reference for age used can be found in Rieke et al. (2005).  $\sigma_{R_{60}}$  is the error on the ratio ( $R_{60}$ ) between measured flux and predicted flux based on  $K_s - [24]$  color.  $\mathcal{X}_{60}$  is the significant of excess emission at 60  $\mu\text{m}$ , i.e.,  $(R_{60} - 1)/\sigma_{R_{60}}$ , while the last column is a  $2\text{-}\sigma$  upper limit on  $R_{60}$ , i.e.,  $R_{60} + 2\sigma_{R_{60}}$ .



TABLE 3  
DEBRIS DISK PROPERTIES

Name	$F_{ire,24}$ mJy	$\mathcal{X}_{24}$	$F_{ire,70}$ mJy	$\mathcal{X}_{70}$	$T_{[24]-[70]}$ K	$f_d$
group I – 24 and 70 $\mu\text{m}$ excess disks						
HD014055	87.06	13.1	766.18	4.9	75	6.71e-05
HD019356	209.51	30.6	76.21	6.5	219	3.19e-06
HD002262	18.06	4.5	47.81	12.8	98	7.07e-06
HD023862	588.46	91.9	194.32	8.3	235	3.14e-04
HD027045	12.69	14.6	32.3	4.6	99	1.05e-05
HD028355	29.51	26.8	167.16	30.7	82	5.59e-05
HD030422	7.5	11.7	60.49	59.9	76	4.86e-05
HD031295	33.49	17.3	404.26	87.1	71	4.46e-05
HD038056	16.47	44.5	47.46	44.8	96	4.81e-05
HD038206	75.11	47.5	338.86	26.3	86	1.36e-04
HD038678	529.07	30.8	210.73	8.6	206	9.75e-05
HD039060	6959.86	9.6	12956.2	7.1	108	1.42e-03
HD071043	26.51	18.4	93.8	3.2	91	4.74e-05
HD071155	91.95	22.3	188.44	68.3	105	2.51e-05
HD075416	85.03	65.9	30.38	32.7	221	4.74e-05
HD079108	19.87	17.1	81.57	32.4	88	4.97e-05
HD080950	81.9	53.5	55.68	58.0	154	7.48e-05
HD095418	226.4	16.0	334.27	4.0	116	1.27e-05
HD097633	62.37	25.1	39.24	20.9	160	7.09e-06
HD102647	457.38	31.2	551.69	12.1	123	1.99e-05
HD106591	38.37	9.3	24.58	6.5	159	4.95e-06
HD110411	47.66	39.4	238.03	107.2	84	3.69e-05
HD111786	15.79	14.4	64.29	17.6	88	2.95e-05
HD115892	118.24	49.1	35.96	5.6	250	1.13e-05
HD125162	75.08	32.4	343.5	88.5	86	5.06e-05
HD136246	3.34	15.2	33.11	23.5	73	4.78e-05
HD139006	383.07	24.8	445.81	5.5	125	1.43e-05
HD158460	7.12	20.9	13.25	11.1	108	5.26e-06
HD161868	173.41	9.5	1058.6	4.9	81	7.52e-05
HD165459	8.06	32.2	24.03	22.2	95	4.66e-05
HD172167	955.95	10.7	10553.6	4.6	72	2.33e-05
HD181296	308.69	47.8	400.36	9.7	120	1.97e-04
HD183324	5.13	4.1	25.87	5.3	84	1.04e-05
HD216956	608.31	3.2	8697.54	11.8	70	6.14e-05
HD221756	9.69	9.0	35.82	13.4	90	1.92e-05
HD225200	11.49	16.4	98.51	41.7	75	7.95e-05
group II – only-70 $\mu\text{m}$ excess disks						
HD004150	...	...	10.06	4.5	<119	<2.24e-06
HD011413	...	...	46.99	21.9	<66	<2.54e-05
HD028226	...	...	100.03	9.9	<60	<3.51e-05
HD028527	...	...	24.65	4.1	<83	<6.27e-06
HD033254	...	...	13.66	6.3	<93	<6.07e-06
HD108382	...	...	14.21	11.6	<85	<4.23e-06
HD188228	...	...	50.29	8.2	<61	<1.19e-05
HD198160	...	...	54.86	9.5	<61	<1.34e-05
group III – stellar photospheres						
HD015008	...	...	...	...	<249	<1.37e-06
HD016970	...	...	...	...	<114	<1.49e-06
HD076644	...	...	...	...	<170	<1.44e-06
HD080007	...	...	...	...	<361	<1.07e-06
HD082621	...	...	...	...	<141	<8.84e-07
HD083808	...	...	...	...	<125	<6.80e-07
HD087901	...	...	...	...	<83	<4.70e-07
HD103287	...	...	...	...	<322	<2.41e-06
HD108767	...	...	...	...	<146	<5.30e-07
HD112185	...	...	...	...	<244	<1.31e-06
HD112413	...	...	...	...	<341	<2.94e-06
HD116842	...	...	...	...	<99	<1.67e-06
HD130841	...	...	...	...	<140	<8.79e-07
HD135742	...	...	...	...	<84	<4.10e-07
HD209952	...	...	...	...	<205	<9.16e-08
HD210418	...	...	...	...	<130	<1.57e-06
HD214923	...	...	...	...	<147	<4.21e-07
HD215789	...	...	...	...	<108	<1.40e-06
HD216627	...	...	...	...	<93	<1.61e-06